QATAR UNIVERSITY

COLLEGE OF ARTS AND SCIENCES

THERMOELECTRIC BEHAVIOR OF NANOCRYSTALLINE TIN SELENIDE NANOCOMPOSITES

BY

MARIEM CHAMAKH

A Thesis Submitted to the Faculty of

the College of Arts and Sciences

in Partial Fulfillment

of the Requirements

for the Degree of

Masters of Science

in

Material Science and Technology

June 2018

COMMITTEE PAGE

The members of the Committee approve the Thesis of Mariem Chamakh

defended on 05/06/2018.

_____

Dr. Khaled Youssef
Thesis/Dissertation Supervisor

_____

Dr. Khalid Al-Saad
Committee Member

_____

Dr. Ahmed Ayesh
Committee Member

_____

Dr. Adel Mohamed
Committee Member

Approved:

_____

Rashid Al-Kuwari, Dean, College of College of Arts and Sciences

ABSTRACT

CHAMAKH, MARIEM, M., Masters : June : 2018, Material Science and Technology

Title: Thermoelectric Behavior of Nanocrystalline Tin Selenide Nanocomposites

Supervisor of Thesis: Khaled, M, Youssef.

Thermoelectric technology converts thermal energy to electricity. Many studies were conducted on thermoelectric materials such as Bismuth Telluride and Lead Telluride. And the goal was to achieve an average ZT >2 which is required for waste heat recovery applications. Recently Tin Selenide (SnSe) showed a promising performance with a ZT of nearly 2.6 at 923 K for its single crystal structure at the b-axis. However, single crystal SnSe is very fragile and the production of single crystal SnSe structure is a complicated and costly process. Therefore, great interest was given to polycrystalline SnSe.

In this work, the thermoelectric performance of polycrystalline SnSe was enhanced through nanostructuring and nano-composting with graphene via a cost-effective methodology. Nanocrystalline SnSe composites were successfully prepared by high energy ball milling and SPS techniques, and the structural characterization by X-ray Diffraction and Transmission Electron Microscopy revealed that the average grain size of both pristine SnSe and SnSe with Graphene was approximately (~ 10 nm). The mechanical properties were evaluated and showed an enhancement with high hardness values. The nanostructuring contributed in the enhancement of Seebeck coefficient and the highest reported value so far was obtained for pristine SnSe with 1032 μV/K at 873K. A significant improvement in ZT value was observed for the pristine nanostructured SnSe with a value of 0.9 at 873 K, and the addition of Graphene increased the ZT to 1.2 at 873 K due to the

increased power factor and the lower thermal conductivity. Graphene was detected to be mainly present around the grain boundaries and this finding represents the first ever reported evidence to identify the location of graphene in a nanocrystalline TE material.

DEDICATION

This Thesis is dedicated to my parents and my family, thank you for showing unconditional support and motivation to pursue my goals

ACKNOWLEDGMENTS

I would like to express my sincere gratitude to my supervisor Dr. Khaled Youssef for his support and guidance in my research and writing of this thesis. I would like to thank my committee members Dr. Ahmad Ayesh, Dr. Khaled AlSaad, and Dr Adel Mohamed for their advice and contribution.

My sincere appreciation is extended to the faculty members of Materials Science and Technology program at Qatar University; Dr. Ahmed Elzatahry, Dr. Talal Altahtamouni, and Dr. Aboubakr Abdullah, they have enriched and strengthened my knowledge in this field and helped me in maintaining excellent academic performance.

My great and sincere appreciation goes to Prof. Mariem Al-Maadeed for giving me the chance to explore the research world and introducing me to the materials science, and for showing her constant support for development of achievement. Thanks goes as well to Dr. Deepalekshmi Ponnama for guiding me and teaching me the fundamentals of research. Special thanks to Dr. Leena AlSulaiti for her support during my master's study years.

I would like to thank the staff of Center for Advanced Materials CAM and Central Laboratory Unit CLU for their cooperation during my research period.

Financial support by Qatar University student grant number QUST-1-CAS-2018-19 is gratefully acknowledged.

TABLE OF CONTENTS

LIST OF TABLES

LIST OF FIGURES

CHAPTER 1: INTRODUCTION

The world is currently facing numerous issues related to energy and environment. Energy consumption is rapidly increasing with the technological advancements and population growth. The U.S Energy Information Administration projected the increasing trend of world energy consumption by energy source as presented in Figure 1.1 [1]. In addition to the necessity of providing environment friendly renewable sources to meet this growing consumption, there is an important issue that must be considered, that is much of the produced energy is actually lost in vain. In fact, only one third of the produced energy is used effectively and the two-thirds is being lost in the form of waste heat. In the U.S alone, an equivalent of 46 billion gallons of gasoline is wasted annually from around 200 million light-duty vehicles exhaust pipes. Also, an equivalent of 1.72 billion barrels of oil is lost in form of waste heat energy in the manufacturing sector each year [2]. Therefore, Technology for recovering the waste heat is very essential and it is one of the best energy saving methods to achieve efficiency and environment security.

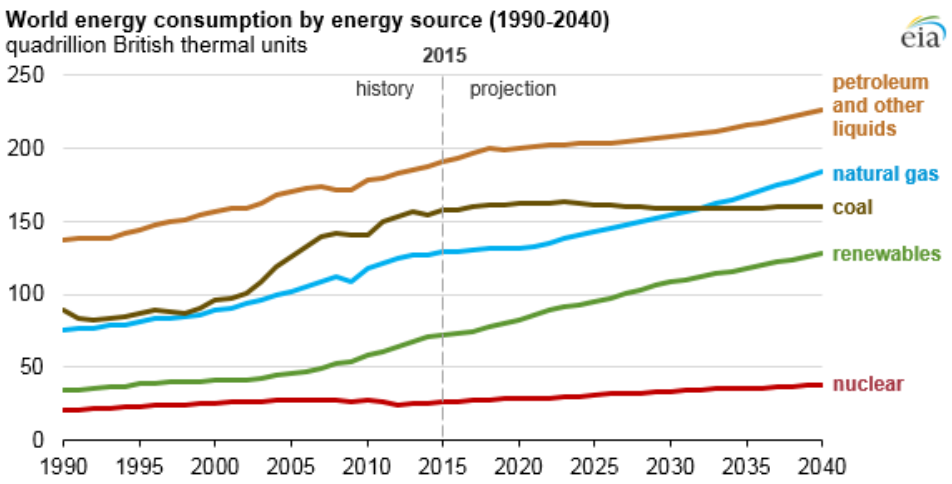

Figure 1.1 World energy consumption by energy source (1990-2040) [1].

Thermoelectricity represents a promising waste heat recovery technology. It is based on the direct conversion of heat to electricity by the Seebeck effect. This energy-conversion phenomenon plays a key role in developing cost effective, pollution-free alternative energy technologies. Thermoelectric energy converters can be used to transform heat from many heat sources such as power plants, factories, motor vehicles, and electronic devices. This solid-state technology provides several advantages, such as the absence of chemical reactions and toxic residuals, the long-life span of reliable operation with reduced cost of maintenance. Advantage of simplicity as they produce no vibrations and are highly scalable, and the lack of moving parts [3][4][5]. This great potential of thermoelectric materials was a motivation to expand the search for novel materials with higher efficiency, which is evaluated by the figure of merit ZT. Bismuth Telluride and Lead Telluride have been the pioneer in the thermoelectric research and a lot of focus was given to increase

their ZT value over the years, with many strategies adapted like doping and nanostructuring. However, the presence of lead and the use of the costly telluride has limited their future in domestic applications.

Recently, Tin Selenide SnSe has emerged as an excellent thermoelectric material for being earth abundant and environmentally friendly, and for its high electrical conductivity, ultralow thermal conductivity of less than 0.6 W/mK and high Seebeck coefficient of more than 520 µV/K at room temperature, which is higher than Te-based inorganic materials, PbTe, and Bi_2Te_3 [6][7]. In 2014, Zhao et al. [8] reported the exceptional ZT value of 2.6 at 910 K in the b-direction of the single crystal SnSe. Despite the promising thermoelectric performance of the SnSe single crystal, its poor mechanical properties are a limitation for device fabrication, in addition to its complex and high-cost growth technology. So, more attention has been switched to the polycrystalline because of its good mechanical properties and easily controlled production.

The objective of this work is to enhance the thermoelectric performance of SnSe through nanostructuring and nano-composting with graphene via a cost-effective methodology. This report represents the fabrication methodology of pristine SnSe and Graphene-SnSe nanocomposite via high energy ball milling method followed by powder consolidation by Spark Plasma Sintering SPS. All the characterization techniques are described as well, in which the structural properties of the samples were investigated by XRD and TEM, the mechanical and thermal properties were evaluated by Microhardness and DSC, thermoelectric properties were measured to calculate the efficiency ZT, and the elements distribution was performed by STEM. The analysis of the results is presented in

chapter 4 of this report, and it showed the successful fabrication of nanostructured composite with enhanced and a promising thermoelectric performance with an exceptional high Seebeck coefficient.

CHAPTER 2: LITERATURE REVIEW

2.1 Thermoelectric effect

Thermoelectric technology is playing an important role for power generation and cooling devices and it is based on the energy conversion interplay between temperature gradient and electricity [9]. Thermoelectric effect includes three phenomena which are: Seebeck effect, Peltier effect, and Thomson effect. And the thermoelectric efficiency is governed by the figure of merit ZT.

2.1.1 The Seebeck effect

The Seebeck effect phenomenon was discovered in 1821 by the German physicist Thomas Johann Seebeck [10] . He explained the effect caused by an applied temperature difference, as the diffusion of the charges carriers in the material (electrons and holes) from the hot side to the cold side resulting in a built-in electric field. He discovered this phenomenon when a closed cycle jointed by two different metals with a temperature difference between junctions caused a nearby compass needle to be deflected [10]. The magnitude of this effect is gauged by the Seebeck coefficient or thermopower, which is the thermoelectric voltage developed per unit temperature difference in a conductor, expressed in units of V/K. This effect can only be exhibited in a thermocouple with two different materials which have different Seebeck coefficients [4]. This effect can be mathematically expressed by

$$\Delta V = S_{AB}\Delta T \tag{2.1}$$

Where ΔV is the voltage developed between two dissimilar metals A and B connected by a junction at the cold point as shown in the Figure 2.1 and S_{AB} is the Seebeck coefficient

of the thermocouple with S_{AB}= S_B - S_A, and ΔT is the temperature difference between the hot point and the cold point [11][12][13].

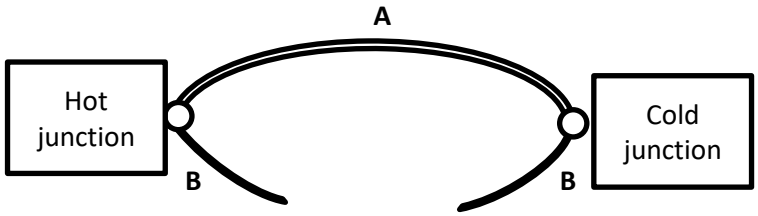

Figure 2.1 Basic Thermocouple.

2.1.2 The Peltier effect

The effect was first discovered by J Peltier in 1834 [11]. Opposite to Seebeck effect which is self-generated, Peltier effect is generated when a voltage is applied to a thermoelectric couple. The current that passes through the junction of two dissimilar metals make the carriers tend to return to the equilibrium by absorbing energy. This energy absorbed is related to the electrical current by the following equation [14][11][15]

$$Q = -\pi_{ab} J_{ab} \tag{2.2}$$

Q: The heat absorbed from the ambient.

π_{ab}: The Peltier coefficient for a junction of materials a and b.

J_{ab}: The current flowing through the junction from material a to b.

2.1.3 The Thomson effects

The Thomson effect describes both Seebeck and Peltier effect, it explains the absorption or release of heat in a homogeneous single conductor that carries an electric current and subject to a temperature gradient where heat is liberated if an electric current flow in the same direction as the heat flows, otherwise it is absorbed [16]. The rate of heat production can be given by the following equation [17]

$$Q^{\cdot} = \rho J^2 - \mu J \nabla T \tag{2.3}$$

Where ρ is the resistivity, J is the current density, μ is the Thomson coefficient.

Knowing the Thomson coefficient allows for the determination of the Seebeck and Peltier coefficient of a material independently at a specific temperature from the kelvin relation [17]

$$\mu = T\frac{dS}{dT} \tag{2.4}$$

$$\pi = TS \tag{2.5}$$

Thomson effect has been used to determine the absolute Seebeck coefficient of lead (Pb), which serves as a reference for all other materials at temperature up to room temperature [12].

2.1.4 The efficiency figure of merit ZT

The performance of thermoelectric materials is evaluated by a dimensionless quantity called the figure of merit which is defined by

$$ZT = \frac{S^2\sigma T}{k} = \frac{S^2 T}{k\rho} = \frac{S^2 T}{(k_e + k_l)\rho} \tag{2.6}$$

Where S is the Seebeck coefficient, σ is the electrical conductivity, T is the temperature

difference, ρ is the electrical resistivity, and k is the thermal conductivity defined by the summation of the electronic thermal conductivity k_e and the lattice thermal conductivity k_l [18][19].

According to the figure of merit equation, high efficiency is achieved with a high Seebeck coefficient and electrical conductivity to create high voltage output, and a low thermal conductivity to maintain a significant temperature gradient [20]. The strong correlation between these parameters as a function of several material factors such as the band structure and carrier concentration, has hindered the improvement of the ZT quantity. Some of the traditional commercial thermoelectric such as Bi_2Te_3 and PbTe possess a ZT value of nearly 1. However, for practical use this value should be higher than 2 [4] [5].

2.2 Thermoelectric parameters

2.2.1 The Seebeck coefficient (Thermopower)

The magnitude of the Seebeck effect is measured by the Seebeck coefficient which is defined as the thermoelectric voltage developed per unit temperature difference in a conductor with unit V/K (or µV/K or µV/^{o}C). The Seebeck effect is a bulk property and only the Seebeck voltage difference can be measured. Different materials have different coefficients, most metals have a Seebeck coefficient of 10 µV/K or less. For example, iron has a Seebeck coefficient of 19 µV/^{o}C at 0 ^{o}C and constantan (copper-nickel alloy) has a negative value of -35 µV/^{o}C at 0 ^{o}C. Semiconductors have higher coefficient of 100 µV/K which makes them suitable for the construction of thermocouples. In general, to achieve a ZT higher than 2, the thermopower should reach a value higher than 225 µV/K [4] [17] [12].

2.2.2 Thermal conductivity

The thermal conductivity of a material comes from the heat transported by electrons and holes (K_e) and the from the phonons traveling through the lattice (K_l). The lattice thermal conductivity is determined by the structure, rigidity, atomic masses, and other characteristics of the lattice. The electronic thermal conductivity is related to the electrical conductivity by the Wiedemann-Franz law [4] [5]:

$$\frac{K_e}{\sigma} = L_o T \tag{2.7}$$

where $L_o = 2.44 \times 10^{-8}$ $(\frac{K^2}{V^2})$.

2.2.3 Electrical resistivity

This material-dependent property is a function of temperature. Its value at room temperature characterize the material of being insulator (10^6 Ωm or more) or a conductor (10^{-6} Ωm or less) while the resistivity of semiconductors falls in between. For a good performance thermoelectric material, the optimum resistivity range is from 10^{-3} Ωm to 10^{-2} Ωm. The variation of electrical resistivity depends on the carriers' concentration and their mean free path. The lattice of a semiconductor should have a nearly infinite conductivity at low temperatures to achieve a low electrical resistivity, which is not the case due to the limited number of free electrons [4] [17].

The thermoelectric properties S, σ, and κ are interdependent as shown in Figure 2.2 which makes the improvement of merit ZT a great challenge.

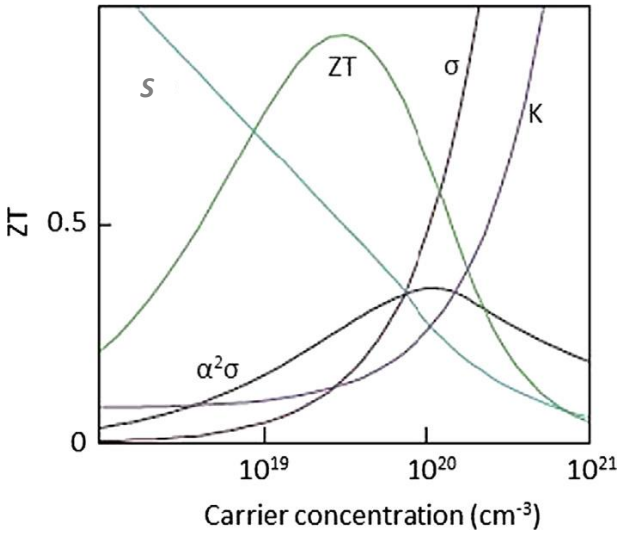

Figure 2.2 Interdependency of thermoelectric properties [4].

2.3 Thermoelectric materials Development

The thermoelectric performance of devices depends greatly on the material used and its properties. Thermoelectric materials comprise a huge family, there exist a wide variety of materials ranging from semimetals, semiconductors, to ceramics. These materials have different structures and crystalline forms, from single crystalline and polycrystalline to nanocomposites. Metal thermocouples were used in the early applications of the thermoelectric effect. However, metals have very high electrical and thermal conductivity which decreases the performance. Interest was switched to semiconductors based thermoelectric materials back in 1930s, for having a greater ratio of thermal conductivity to electrical conductivity compared to metals. The thermoelectric scientific basis was well established in 1950s as the field of thermoelectric started to advance rapidly [21] [16].

The first generation of thermoelectric materials can be categorized to low

temperature materials such as Bi_2Te_3, intermediate temperature materials such as PbTe, and high temperature materials such as SiGe [22]. Bismuth Telluride is a simple and commonly available thermoelectric material and it exhibit a ZT value close to 1. It has an energy gap of 0.13 eV and melting temperature of 585^{o}C. Lead Telluride on the other hand exhibits a lower ZT value, but it shows better chemical stability at higher temperatures when compared to Bi_2Te_3. Its melting point is 923^{o}C with an energy gap of 0.32 eV. SiGe can yield a large power factor since both elements Silicon and Germanium have high lattice conductivities and high carrier mobilities [17][16].

The history of thermoelectric materials can be characterized by the progress in increasing the ZT value as shown in Figure 2.3. The performance of thermoelectric materials can be controlled by the crystal structure, microstructure, densification, and grain orientation and size. These parameters can be used to approach the interdependency challenge between the thermoelectric parameters preventing the enhancement of ZT value [23] . In 1960s the development of these materials to obtain higher ZT values was mainly focused on doping and forming solid solutions, such as Bi_2Te_3–Sb_2Te_3, PbTe–SnTe, and $Si_{1-x}Ge_x$. The aim of this approach was to introduce point defect scattering, thus reducing the lattice thermal conductivity [23][24]. In the later years, more focus was given to find new approaches for the development of the next generation of thermoelectric materials. One of the approaches was based on the use of materials with complex crystal structures, which gave rise to the concept of ‘‘phonon-glass electron-crystal’’ (PGEC). Phonon-glass electron-crystal describes the best thermoelectric material that should have a low lattice thermal conductivity of a glass-like material, and a high electrical conductivity of a crystalline material. Typical examples of these materials are Skutterudites, Clathrates, and

β-Zn_4Sb_3[25] [16]. Another enhancement approach is the synthesis of low dimensional systems by nano structuring. This technique has revolutionized the field and gained a lot of focus in recent years [26] [19][27].

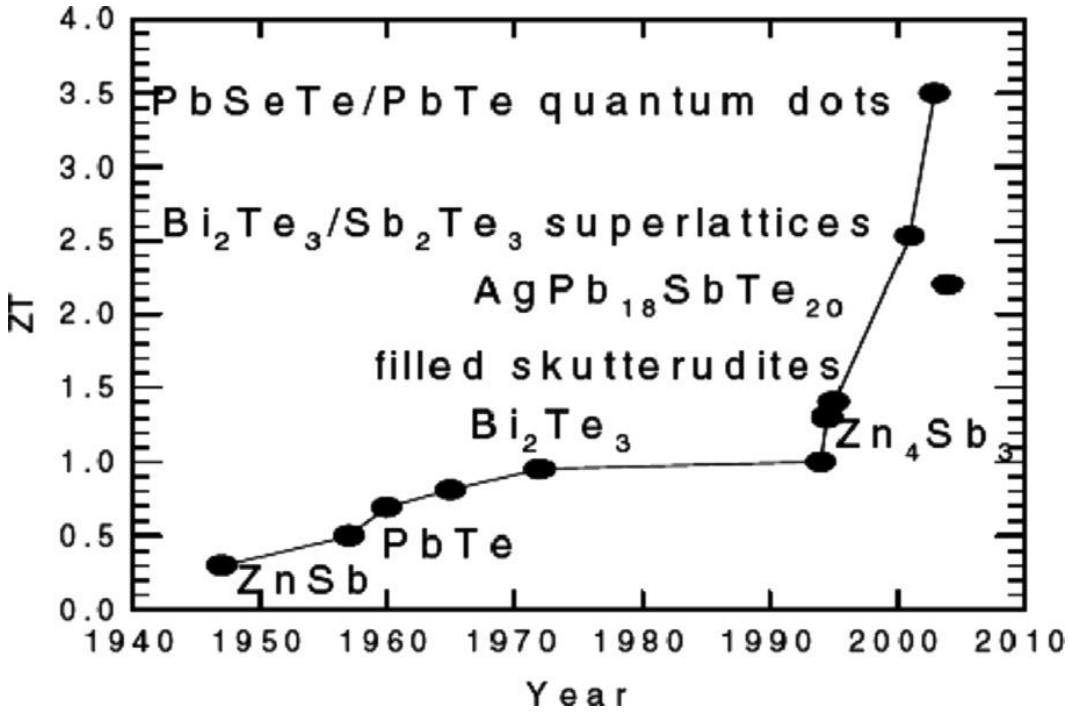

Figure 2.3 ZT of many typical thermoelectric materials as a function of year [4].

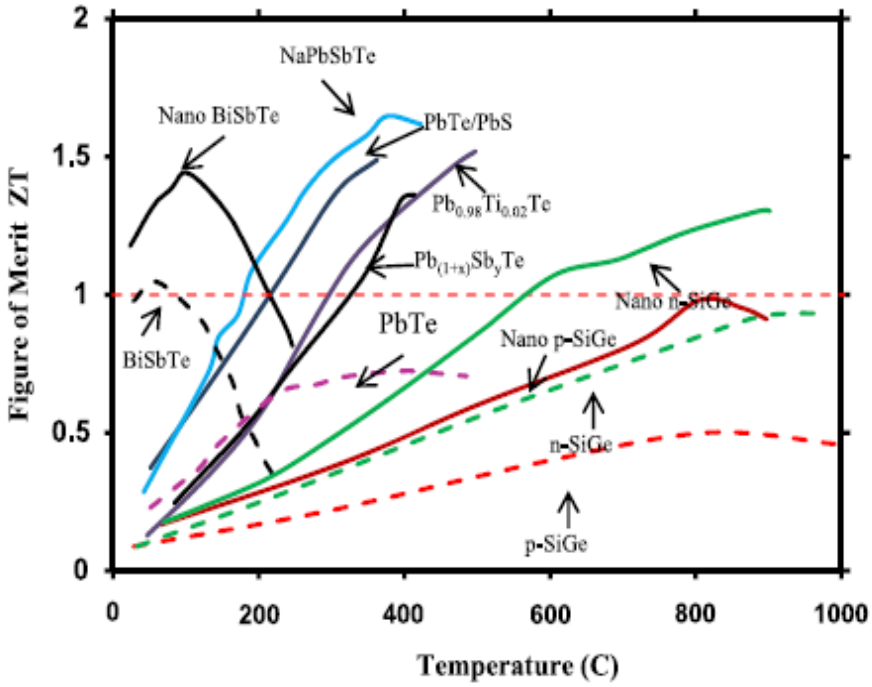

Figure 2.4 ZT Values of TE materials are plotted as a function of temperature [5].

2.4 Nanostructured Thermoelectric Materials

2.4.1 Nano structuring concept

Nano structuring is based on introducing large density of interfaces, where phonon scattering can happen over a large mean-free path range while maintaining the carrier mobility values. This will reduce the lattice thermal conductivity in the thermoelectric material resulting in the enhancement of ZT value [24]. The concept was demonstrated in the 1980s by Rowe et al., the research team was able to reduce the grain size of $Si_{0.80}Ge_{0.20}$ to a few microns, and the results showed a reduction in lattice thermal conductivity by 20% [28]. A theoretical study was conducted which demonstrated the relation between phonon

scattering and lattice thermal conductivity as a function of the mean-free path of Si. The calculations revealed that to achieve a 90% reduction in lattice thermal conductivity, the grain size should be in the range of 20 nm [29]. These dimensions vary for different materials but they remain in the nanoscale [24].

2.4.2 Nano structuring techniques

Various synthesis methods were used to produce practical materials with good control at the nanoscale method. Some of the most common are ball milling, and solvothermal/hydrothermal reaction. These synthesis methods are usually followed by consolidation and densification processes such as cold pressing, hot pressing, and spark plasma sintering. These processes assure to maintain good electrical and mechanical properties achieved at full theoretical density of a material [24] [5].

Ball milling: It is a mechanical alloying technique, where the elemental powders are loaded into a vial with a certain ratio of milling balls. These balls are made of either stainless steel, tungsten carbides, or zirconia. The agitation of the container in the milling machine causes the collision of balls and powder and the release of high energy resulting in the fracture of the material and formation of the nanostructure. The milling process is usually conducted under argon atmosphere to prevent oxidation. This techniques has attracted much attention due to its simplicity, and was employed on SiGe, $FeSi_2$, PbTe, $(Bi,Sb)_2Te_3$, and skutterudites systems [5][24]. The work conducted on SiGe by using high energy ball milling yielded an enhancement in ZT value by 20% [28].

Solvothermal/hydrothermal reaction: In this method a stochiometric ratio of precursor materials are dissolved in a solvent or an aqueous solution with the presence of

a reducing agent. The reaction happens in a sealed autoclave at high temperature for a specific period of time. This method has been effective for many years and been used to produce nanostructured Bi_2Te_3 and PbTe. It showed a good control of morphology and particle size distribution unlike the ball milling technique [24].

The following are the consolidation techniques that usually follows the synthesis processes:

Cold-sintering: this process is suitable for low melting materials such as Bi_2Te_3 and PbTe. It consists of applying hydrostatic pressure of around 5 tons to the materials loaded into a die. Then the compacted material is heated up to 70% of its theoretical melting point [5][24].

Hot-pressing: In this technique the heating is applied simultaneously with the pressure, which can accelerate the densification and fine-grained compact samples can be obtained. The samples can reach up to 95% to 100% of their theoretical density [5][24].

Spark Plasma Sintering: It is similar to the hot pressing; however, the high temperature is achieved quickly by conducting a pulsed direct current through the graphite die while applying hydrostatic uniaxial pressure. It is a very fast process which gives the advantage of preventing grain growth of the nanoparticles [5][24].

2.5 Thermoelectric SnSe

Tin selenide SnSe is a group (IV-VI) semiconductor with a narrow indirect band gap of 0.9 eV at room temperature and direct band gap of 1.3 eV at high temperature [30]. This compound has raised a lot of interest in recent years for being earth abundant and environmentally friendly, and it has been reported as an alternative for the Lead-Cadmium based chalcogenides and ternary I-III-VI group semiconductors such as $CuInS_2$, $CuInSe_2$, and $CuIn_xGa_{1-x}Se_2$ [31]. This material has exhibited promising results for different

applications such as solar cells, lithium ion batteries, infrared optoelectronics, supercapacitors, and memory switching devices [31][6]. It is also a potential candidate for power generation from waste heat given its high electrical conductivity, ultralow thermal conductivity of less than 0.6 W/mK and high Seebeck coefficient of more than 520 µV/K at room temperature, which is higher than Te-based inorganic materials, PbTe, and Bi_2Te_3 [6][7].

2.5.1 SnSe Single Crystal structure

Tin Selenide SnSe possess an orthorhombic layered structure consisting of two atoms thick rock salt slabs, resembling a distorted NaCl structure. The two layers form zigzag projection along the b-axis as shown in Figure 2.5. This double layer (along the b-c plane) is held by a network of covalent bonds, while the Sn-Se bonding between the different double layers in the a- direction is held by van der Waals interactions. Due to this structure SnSe single crystal cleaves easily along the (001) plane leading to poor mechanical properties. In addition, this structure leads to anisotropy where b and c directions show better electrical and thermal conductivity than a-axis direction [32].

The structure of SnSe was first described by Okazaki & Ueda (1956) to be from the space group *Pnma* with lattice parameters a=11.49^o, b=4.44^o, c=4.135^o at room temperature [33]. Studies have shown that phase transition occurs at higher temperatures of around 800^{o}C, leading to a more symmetric structure of group *Cmcm* as described by Wiedemeier & Schnering (1978) and Wiedemeier & Csillag (1979), and it results in a decrease of the band gap and increase in the carrier concentration [34][35].

The complex crystal structure and high temperature phase transition raised attention

to explore the electrical transport properties along all axial directions at different temperatures. This has demonstrated the possible use of SnSe in thermoelectric applications after it has been historically ignored. In fact, Zhao et al. reported a record 2.6 ZT value at 923 K along the b- axis direction with an intrinsically ultralow thermal conductivity of <0.25 W/mK at temperatures above the phase transition of 800 K. This study also showed a high ZT value of 2.3 along the c- axis while the a- axis ZT was significantly low with a value less than 0.8 as shown in Figure 2.5 [8].

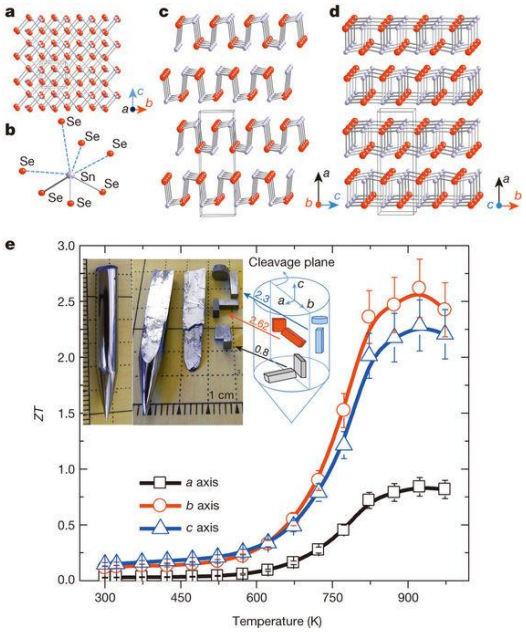

Figure 2.5 SnSe crystal structure Pnma and ZT values. a, Crystal structure along a axis: grey, Sn atoms; red, Se atoms. b, Highly distorted SnSe7 coordination polyhedron with three short and four long Sn–Se bonds. c, Structure along the b axis. d, Structure along the c axis. e, Main panel, ZT values along different axial directions [8].

More studies to develop the thermoelectric performance have been carried out for the single crystal structure. A ZT value of almost 2 was reached at 773 K with the successful hole doping using sodium as an acceptor. Zhang et al. showed that this high performance is due to the increase in the power factor with the increase of electrical conductivity and the strongly enhanced Seebeck coefficient. The authors reported a high device ZT_{dev} of 1.34 in temperature range from 300 K to 773 K which outperforms the un-doped SnSe reported in 2014 at this device temperature range [36] . A recent theoretical study conducted by Li et al, revealed that a maximum ZT value of 4.35 can be reached at 923 K along the b-axis direction for a carrier concentration of 1.82×10^{19} cm^{-3} [37].

2.5.2 Thermoelectric properties of Polycrystalline SnSe

Although single crystal SnSe showed promising thermoelectric performance, its poor mechanical properties are a limitation for device fabrication, in addition to its complex and high-cost growth technology. Therefore, more attention has been switched to the polycrystalline materials because of its good mechanical properties and easily controlled production. Tyagi et al.[38] studied the mechanical properties of polycrystalline SnSe prepared by vacuum melting technique followed by spark plasma sintering for consolidation. The results obtained reveal good mechanical behavior that is comparable with other state of the art thermoelectric materials. In fact, the authors reported measured fracture toughness of 0.76 MPa, and hardness value of 0.27 GPa, and thermal shock resistance of nearly 252 W/m [38]. Polycrystalline SnSe however, shows lower thermoelectric efficiency compared to single crystal because of its low electrical transport properties, such as the Seebeck coefficient and electronic conductivity, originating from

the very low intrinsic carrier concentration. The number of carriers is affected by the defects and minor impurities introduced by the synthesis method. Sassi et al. reported a maximum ZT value of 0.5 at 823 K for polycrystalline SnSe prepared by a sealed melting technique followed by SPS [39]. Another shortcoming of polycrystalline SnSe processing are the inhomogeneous phases causing the frequent segregation of Sn. Y.Li et al. [40] studied the high temperature oxidation behavior of thermoelectric SnSe, and the results showed the rapid oxidation to SnO_2 at high temperatures of 600ºC and 700ºC. They concluded from their study the need of vacuum or a protective coating for the efficient use of SnSe [40]. Many studies were conducted to enhance the performance and fabrication of polycrystalline SnSe, which include nano-structuring and texture modulation, and elemental doping.

2.5.2.1 Nano-structuring and texture modulation

Nano-structuring has been used recently to enhance the conversion efficiency of thermoelectric materials. The reduction of grain size increases the phonon scattering thus decreases the thermal conductivity. Sanchez et al.[41] introduced a straightforward preparation procedure for highly oriented polycrystalline SnSe. The authors used the arc melting technique, which allowed the production of a highly textured nanostructure. They reported an extremely low thermal conductivity of 0.1 W/mK at 395 K, which was explained by the increase of phonon scattering. The results also showed an increase in Seebeck coefficient with temperature reaching a record value of 668 µV/K at 380 K, which is higher than the reported values by Zhao et al [42] [8]. Another nano-structuring technique is hydrothermal method followed by sintering in an evacuated and encapsulated ampoules. This technique was used by Chen et al. [43] and they were able to synthesis

nanostructured SnSe with enhanced electronic transport properties and low thermal conductivity. These properties were investigated with the change in reaction temperature, duration, and sintering temperature as shown in Figure 2.6. The results showed that a large power factor of 2.28 $\mu W/cmK^2$ can be reached at 550 K if the samples are synthesized at a reaction temperature of 170^oC and sintered at 580^oC. Also, a significant improvement of ZT value was observed for samples sintered at 500^oC reaching 0.54 at 550 K, which was explained by the low thermal conductivity achieved by the nano-structuring of the material [43].

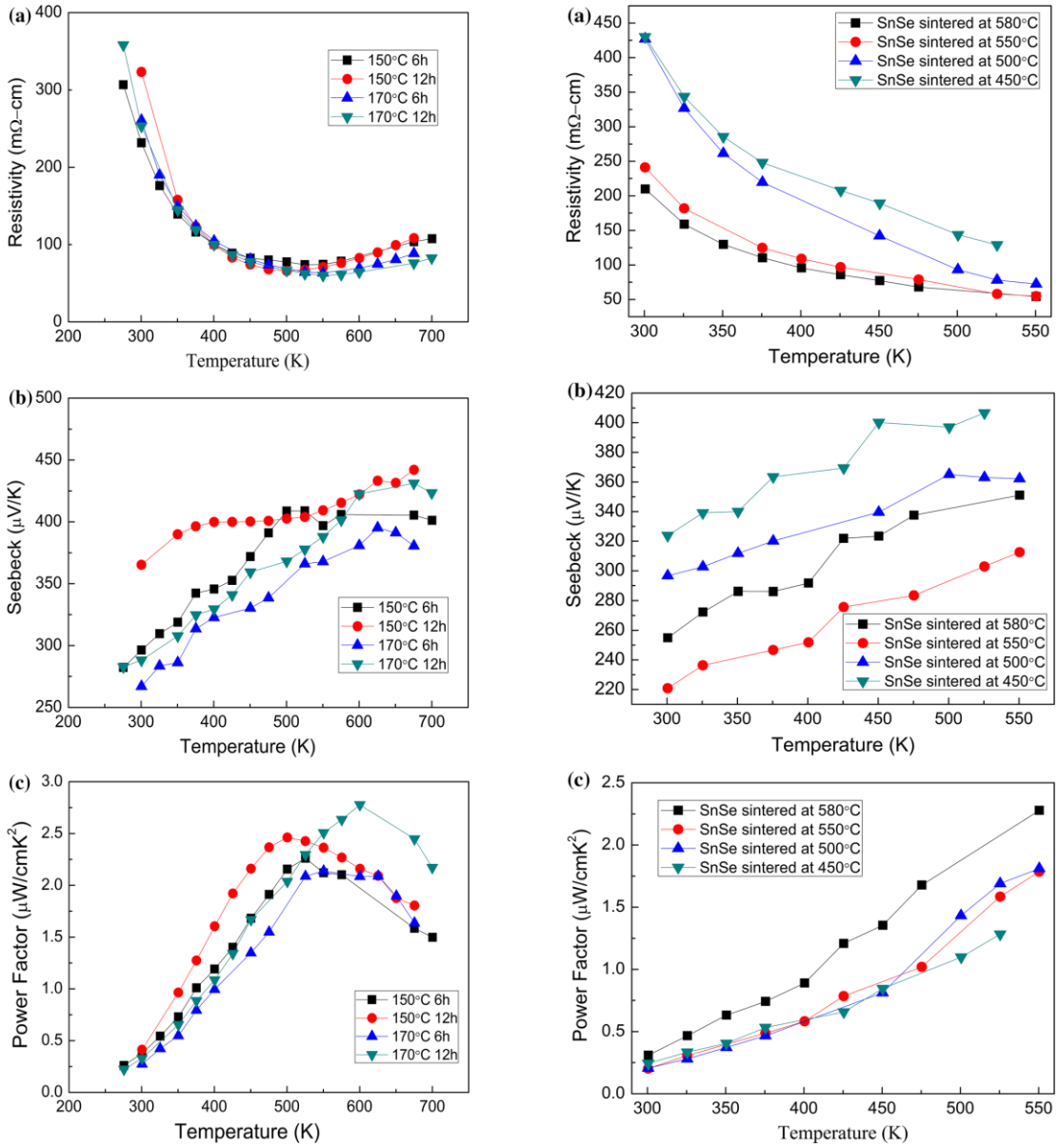

Figure 2.6 a). Temperature dependence of electronic transport properties for hydrothermally synthesized SnSe at 150–170 ºC for 6–12 h, followed by evacuating-and-encapsulating sintering at 580 ºC ; b).Temperature dependence of electronic transport properties for hydrothermally synthesized SnSe at 170 ºC for 12 h, followed by evacuating-and-encapsulating sintering at 450–580 ºC [43].

Some other studies focused on the effect of texturing on the thermoelectric properties which are anisotropic and strongly depend on the grains orientation. The electrical properties are expected to be enhanced if the crystallographic texture is controlled, to assure the alignment of grains along the favorable transport directions. One of the proven strategies for grains orientation is the zone-melting (ZM) method, which was employed by Fu et al. to prepare a highly textured structure of polycrystalline SnSe. The results revealed a maximum power factor of 9.8 $\mu W/cmK^2$ with a peak ZT value of 0.92 at 873 K. the samples were then prepared by SPS technique and a further enhancement of the thermoelectric performance was observed with ZT value higher than 1, and it was explained by the reduction of the lattice thermal conductivity due to the refining of the grain size [44]. Inspired by the work of Y.Fu and co-authors, Feng et al. studied the effect of sintering temperature on the texturing degree. They prepared polycrystalline SnSe nano-powder by hydrothermal reaction and an average ZT value of 0.38 was obtained which is one of the highest average values for polycrystalline SnSe in the temperature range of 300 K to 800 K. and the highest ZT value is 0.81 at 773 K for the sample sintered at 400^{o}C. Figure 2.7 shows the microstructure of the prepared sample examined by TEM. The images reveal the layered structure of SnSe, which caused the significant increase of in-plane phonons scattering, thus the ultralow lattice thermal conductivity as explained by the authors [45].

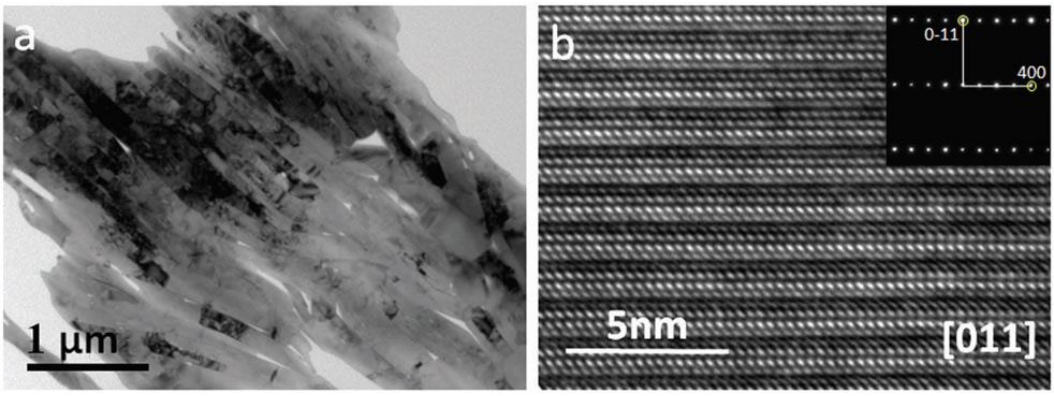

Figure 2.7 (a) Low magnification TEM image of the 450 oC sintered sample view along the direction vertical to the press direction; (b) high-resolution TEM image of the 450 oC sintered sample along the [0 1 1] direction [45].

Table 2.1 represents thermoelectric properties and preparation methods investigated in literature for polycrystalline SnSe.

Table 2.1 Thermoelectric properties of Polycrystalline SnSe

Reference	Preparation method	κ (W/mK)	S (μV/K)	PF (μW/mK^2)	ZT	T (K)
[46]	Milling and Hot pressing	0.2	180	207	0.15	750
[47]	Mechanical alloying and SPS	0.37	300	120	0.27	823
[48]	Hydrothermal method and SPS	0.85	-149	300	0.28	793
[49]	Melting synthesis and HPS	0.69	340	390	0.46	823
[43]	Hydrothermal method	0.18	350	180	0.54	550
[50]	Melting and Hot pressing	0.75	300	540	0.64	873
[51]	Annealing	0.81	320	115	0.11	772
[52]	Zone melting (annealing) and SPS	0.45	430	200	0.35	773
[45]	Hydrothermal reaction and SPS	0.25	310	240	0.80	773
[44]	Zone melting and SPS	0.7	410	840	1.05	873
[53]	Annealing	0.25	260	280	1.10	873
[54]	Annealing	0.61	310	430	0.60	800
[55]	Melting and Hot pressing	0.66	305	570	0.78	910
[30]	Solvothermal reaction and SPS	0.45	340	350	0.60	773
[56]	Annealing	0.5	420	350	0.60	823
[57]	Annealing and SPS	0.73	525	920	1.10	873
[58]	Melting and annealing	0.37	350	270	0.62	823
[59]	Melting and annealing	0.55	325	264	0.37	773
[60]	Mechanical alloying and SPS	0.46	310	370	0.71	873

[61]	Mechanical alloying and SPS	0.48	-250	45	0.09	773
[61]	Mechanical alloying and SPS	0.21	260	170	0.65	773
[61]	Mechanical alloying and SPS	0.48	-500	88	0.15	773
[62]	Hydrothermal method	1.4	160	260	0.06	300
[63]	Melting and SPS	0.4	400	420	0.80	773
[64]	Annealing and SPS	0.62	400	280	0.37	773
[42]	Arc melting	0.1	668	70	0.27	380
[65]	Melting and annealing	0.35	370	250	0.56	790
[66]	Annealing and SPS	0.6	440	275	0.30	750
[39]	Annealing and SPS	<0.5	370	300	0.50	820

2.5.2.2 Elemental doping

Tin Selenide (SnSe) has low intrinsic defect concentration, which motivated researchers to use doping as a means to increase the concentration of free carriers in order to enhance electronic transport properties and reduce the thermal conductivity by the introduction of defects. In 2014, Chen et al. [66] reported a record high ZT value of 0.6 at 750 K for polycrystalline SnSe doped with Ag. The samples were prepared by melting and hot pressing. Ag was chosen by the authors as dopant due to its high stability compared to Na when subjected to repeated heating and cooling. Ag proved also to be able to increase

the carriers' density to concentrations suitable to achieve good thermoelectric performance. In fact, this study showed the increase of carriers' number to 9×10^{18} cm^{-3}. As for Na-doping reported by Chere et al., [67] the carriers' concentration reached nearly 2.7×10^{19} cm^{-3}, resulting in the increase of electrical conductivity and power factor, thus a high ZT value of 0.8 at 773 K was obtained. Tang et al. [53] aimed to enhance two essential factors for thermoelectric performance which are the power factor and the low thermal conductivity. The authors introduced nanoscale precipitate of PbSe, and they were able to achieve a remarkably high ZT of 1.7 at 873 K. The work of Li et al. gave a ZT value of 0.54 at 793 K. The authors introduced n-type dopant of $PbBr_2$ to optimize the thermoelectric properties. They explained the enhanced performance by the role of Br in converting p-type SnSe to n-type, and the effect of Pb in decreasing the thermal conductivity since it has a heavier relative atomic mass [48]. Another effect of doping is the change in band-structure and the band-gap energy which helps in the enhancement of Seebeck coefficient. This effect was reported by Gharsallah et al. [68] where they aimed to enhance the thermoelectric performance of their previous nanostructured SnSe prepared by arc melting. The authors added Ge to their samples and the results showed an extraordinary Seebeck coefficient of 1000 μV/K at low doping concentrations. A very recent study published in 2018 by Gong et al. [69] revealed the effect of Cu doping on thermoelectric efficiency of polycrystalline SnSe. The Cu dopant introduces atomic point defect scattering, that is the cause of the extremely low thermal conductivity which in turn results in ZT value of 1.2 at 873 K.

Table 2.2 introduces the thermoelectric properties of SnSe with different elemental dopants.

Table 2.2 Thermoelectric properties of Doped SnSe

Reference	Material	Preparation method	κ (W/mK)	S (μV/K)	PF (μW/mK^2)	ZT	T (K)
[70]	PbTe-SnSe	Milling and Hot pressing	0.65	275	920	1.25	880
[46]	$LaCl_3$-SnSe	Mechanical alloying and SPS	0.3	350	200	0.55	750
[69]	Cu-SnSe	Hydrothermal method and SPS	0.24	320	340	1.20	873
[47]	Cu-SnSe	Melting synthesis and HPS	0.39	320	378	0.79	823
[71]	Sm-SnSe	Melting synthesis and HPS	0.3	250	214	0.55	823
[48]	$PbBr_2$-SnSe	Melting and Hot pressing	0.73	-363	480	0.54	793
[72]	Na-K-SnSe	Mechanical alloying and SPS	0.32	375	492	1.20	773
[49]	Ge-SnSe	Zone melting (annealing) and SPS	0.67	379	511	0.60	823
[73]	Ti-Pb-SnSe	Mechanical alloying and SPS	0.58	380	300	0.40	773
[50]	Zn-SnSe	Annealing	0.8	330	830	0.96	873
[52]	Br-SnSe	Annealing	0.36	-370	510	1.10	773
[52]	Pb-SnSe	Annealing	0.35	-350	600	1.20	773
[67]	Na-SnSe	Melting and Hot pressing	0.4	250	430	0.80	773
[68]	Ge-SnSe	Arc melting	0.5	850	900	0.7	390
[53]	Sn-PbSe	Hydrothermal Synthesis	0.24	330	460	1.70	873

[54]	Na-SnSe	Melting and annealing	0.51	253	570	0.87	800
[54]	K-SnSe	Melting and annealing	0.44	350	460	0.80	800
[54]	Li-SnSe	Melting and annealing	0.53	255	380	0.55	800
[55]	C-SnSe	Annealing	0.72	330	920	1.20	910
[56]	Na-SnSe	Melting and SPS	0.56	350	480	0.75	823
[58]	In-SnSe	Direct melting and SPS	0.35	350	75	0.20	823
[74]	SnTe-Se	Melting and annealing	0.57	325	1050	1.60	875
[75]	Ge-SnSe	Melting and SPS	0.44	375	430	0.77	800
[59]	Cu-SnSe	Annealing and SPS	<0.24	<230	<120	0.7	773
[59]	Al-SnSe	Annealing and SPS	<0.38	<300	<170	0.6	773
[59]	In-SnSe	Annealing and SPS	0.68	375	80	0.08	773
[59]	Pb-SnSe	Annealing and SPS	<0.45	<310	<200	0.55	773
[76]	SnS-Se	Melting	0.3	475	300	0.82	823
[63]	I-SnSe	Melting and hot pressing	0.3	-640	400	1.00	773
[64]	Na-Te-SnSe	Mechanical alloying and SPS	0.52	280	500	0.72	773
[66]	Ag-SnSe	Melting and hot pressing	0.74	352	560	0.60	750
[77]	Te-SnSe	Tube melting reaction	2.2	170	2000	0.80	860

2.6 Graphene for thermoelectric applications

Graphene is a two-dimensional material composed of a single sheet of carbon atoms arranged in a hexagonal structure, and it is the building block for graphite. It has emerged as a material of enormous interest due to its unique properties. This single layer of material

is well known for being the lightest and strongest material discovered so far. It is characterized by a large surface area, good mechanical properties, exceptional electron transport behavior, high thermal conductivity, and optical transparency. Some of the novel applications of graphene are in the field of optoelectronics, nanoelectronics, energy conversion, and energy storage devices [78][79].

2.6.1 Graphene thermoelectric properties

The study of 2-D systems in the field of thermoelectric was initiated in 1990s, when Hicks and Dresselhaus suggested that low dimensional systems should have a higher ZT value (more than 1) than bulk materials [80]. This enhanced performance comes from the size quantization which increases the Seebeck coefficient, and the interface effects which reduce the thermal conductivity [81].

Graphene has recently attracted significant attention as a potential thermoelectric material because of its electrical and mechanical properties. However, the main obstacle to utilize Graphene as a thermoelectric material is its high thermal conductivity that can reach up to 5000 W/MK. And since it is gapless semiconductor, its Seebeck coefficient is very low ranging from 30-60 µV/K. Therefore, strategies to tune better thermoelectric properties were studied like band engineering [80]. In fact, Dragoman et al. predicted a giant thermoelectric effect in graphene in 2007. The work consisted of calculating the Seebeck coefficient of a graphene-based interface consisting of metallic electrodes periodically patterned over graphene and deposited on a silicon dioxide substrate. The results showed the largest reported Seebeck coefficient with value reaching 30 mV/K [82]. Zeuv et al. conducted thermoelectric properties measurements on a single-layer graphene sheet

exfoliated onto a 300 nm-thick SiO_2 layer grown on degenerately doped Si substrate. The authors obtained a peak value of thermopower of 80 µV/K at room temperature [83]. Another theoretical study was conducted by Ouyang and Guo on graphene nanoribbons. The results showed the effect of the low-dimensional geometry on the thermoelectric properties, where there was an increase in thermopower but decrease in ZT value because of the important reduction in electronic conductivity of the quasi-one-dimensional geometry [84]. Another report about the effect of graphene geometry was conducted by Sevincli et al. [85] Edge-disordered zigzag graphene nanoribbons were investigated, and the results showed the possibility of a PGEC behavior which makes this material promising for thermoelectric applications.

2.6.2 Graphene-based composites thermoelectric materials

Graphene has been recently used for the enhancement of thermoelectric performance of materials with low electrical conductivity and low Seebeck coefficient. Du et al. aimed to develop a low cost thermoelectric material by using Polyaniline benefiting from its low thermal conductivity. To increase its electrical transport properties, Graphene nanosheets were added. The power factor of the nanocomposite was increased from 0.64 to 5.6 µV/K due to the increase in carrier mobility [86]. Graphene has been used as well with some sate-of-the-art thermoelectric materials such as Bi_2Te_3. Liang et al. [87] used hydrothermal method and SPS to prepare Graphene/Bi2Te3 composite material. The authors investigated the effect of graphene on the thermoelectric properties. According to their results the performance was increased 31% compared to the pure BiTe2 when 0.2 vol% of graphene was added at 475 K. Rahman et al. fabricated a thermoelectric device

from n-type and p-type graphene-doped Bi_2Te_3-glycerol hybrid film. The thermoelectric properties were studied and the optimum results were obtained at 0.08 wt% for both n-type and p-type hybrid films with enhanced Seebeck coefficient and electrical conductivity. The results of the fabricated thermocouple device showed an equivalent output power of 24.2 nW [88]. Another study on adding graphene with Bismuth Telluride was conducted by Ju et al. [89]. They prepared nanostructured graphene/Bi_2Te_3 beads composites with ball milling process and graphene/Bi_2Te_3 nanowires with solution-phase synthesis route. As shown in Figure 2.8, the maximum values of the Seebeck coefficient and power factor are obtained at graphene concentration of 0.5 wt% at room temperature. The addition of graphene up to 3 wt% reduce the thermal conductivity because the presence of effective phonon scattering centers. Suh et al. [90] conducted a study on $Bi_{0.5}Sb_{1.5}Te_3$-expanded graphene composites. The authors aimed to enhance both the phonon scattering and electrical conductivity of the material by using the solution-based synthesis method and adding graphene. At a concentration of 0.1 vol% of graphene, the carrier concentration was increased and the power factor was enhanced. A maximum ZT value of 1.13 at 360 K was obtained, which shows a 45 % enhancement compared to the pristine sample. A recent study on graphene/Cu_2SnSe_3 composite was performed by Zhao et al. [91] Ball milling technique was used in the synthesis of the composite material followed by SPS. The graphene sheets acted as phonon scattering interfaces resulting in a reduction of thermal conductivity. This property keeps decreasing up to a certain optimum value of graphene content. The maximum ZT value was 0.44 at 700 K with graphene content of 0.35 vol%.

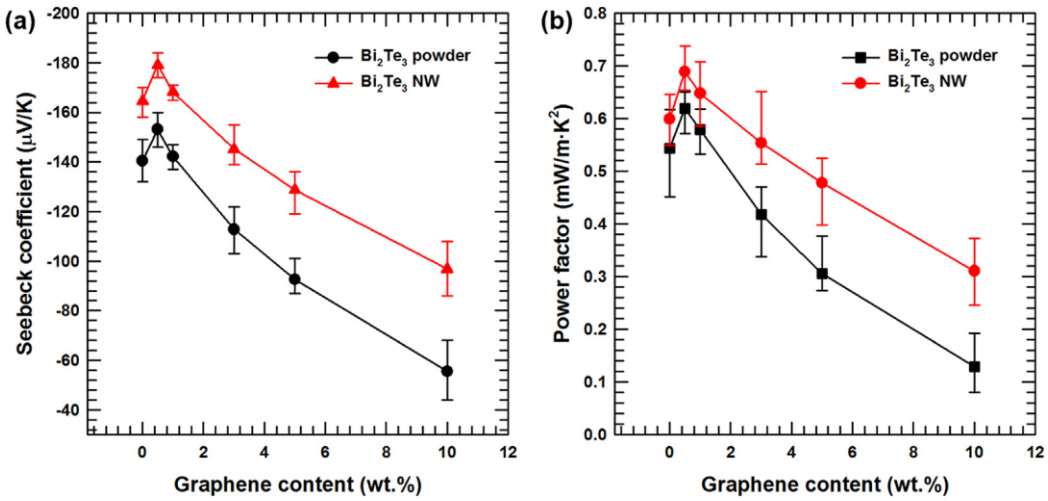

Figure 2.8 (a) Seebeck coefficient and (b) power factor of the synthesized graphene/Bi_2Te_3 composites with different graphene content [89].

CHAPTER 3: EXPERIMENTAL WORK

The experimental work chapter introduces the materials used in this work and the preparation procedure of the nanocrystalline SnSe and the Graphene nanocomposite. It explains the high energy ball milling technique and the spark plasma sintering and the conditions used to prepare the samples. In a second part, all the characterization techniques used to evaluate the structure, mechanical properties, thermal properties and thermoelectric properties of the material are described.

3.1 Materials

The raw materials used are purchased from Alfa Aesar, and consist of high purity Tin powder Sn (99.995 %) of ~100 mesh, high purity Selenium powder Se (99.5 %) of ~325 mesh, and Graphene nanoplatelets.

3.2 Sample preparation

3.2.1 High energy Ball milling

High energy ball milling is a mechanical alloying technique where a mixture of powder particles is subjected to heavy plastic deformation to produce a homogeneous material with reduced particle size. It is a well-established, economic, simple process to produce nano-structured materials with particle size range of 2 to 20 nm. However, some of its disadvantages are the ununiform particle size distribution, and the introduction of defects and contamination. The process consists of loading the powder mixture in stochiometric proportions into the milling container with the grinding medium, the motion of the mill causes the increase of velocity of grinding balls generating the necessary impact force to fracture the powder which is trapped between them as shown in Figure 3.1. During

the process several parameters are controlled and optimized to achieve the desired product and structure. Some of these parameters are the milling time and speed, the grinding medium type and size, the ball-to-weight ratio, and the milling atmosphere and temperature [93][94].

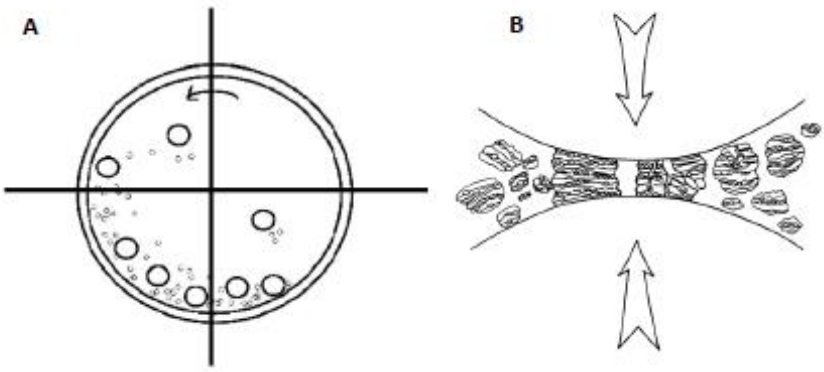

Figure 3.1 Schematic representation of A) The rotation of material inside the milling vial, B) The crushing of materials as a result of balls collisions [94].

There are several types of mills used in the mechanical alloying process, and one of the most commonly used for laboratory investigations is the SPEX shaker mill. The vial containing the powder mixture and the grinding balls is attached by a clamp and swung back-and-forth in a shaking motion. The motion of clamps in this equipment is generally of 1200 rpm allowing the balls to reach a high velocity and collide with high energy to the

powder sample. Generally, the higher the motion speed the higher is the impact energy released on the powder. However, there is a critical speed above which the balls will be pinned to the inner wall of the container and do not fall and collide with the powder. Also, reaching very high speed will cause a high increase in temperature that can affect the structure of the sample or generate a contamination. The time of milling is also critical to reach the desired microstructure which is also related to the other process parameters. Some reports that with increasing milling times the level of contamination increases [94].

This process is highly affected by the grinding medium. The milling balls are generally made of steel and their density is high enough to create the enough collision energy on the powder. Generally, the greater size of the balls generates higher impact force, and some reports predicted that different balls diameters can bring even higher collision energy. The use of a combination of balls with different sizes has been reported to help in reducing the amount of powder coated in the container walls and create shearing forces that detach the powder from the surface of the balls. In addition to the size the balls proportion is an important variable in the milling process. The ball-to-powder weight ratio which is also referred as the charge ratio, has been investigated and varied and it ranged from 1:1 to 220:1. For the SPEX mill, a ratio of 10:1 is generally used. This ratio affects the milling duration, where a higher ratio allows for a faster process. The increase in the weight proportions of the balls causes an increase in collisions per unit time, thus higher energy is transferred to the particles [94].

Another important parameter in the milling process is the atmosphere which highly controls the contamination and oxidation of the powder and its final phase. The milling vials are evacuated and filled with an inert gas, and the most common gas used is high-

purity argon [94].

In this work SPEX SamplePrep 8000M Mixer/Mil shown in Figure 3.2 was used to prepare nanostructured Tin Selenide (SnSe) nanocomposites. According to the phase diagram shown in Figure 3.3, the intermetallic SnSe composition is 50:50. Accordingly, to prepare 5 g of sample, 3.0027 g of Sn and 1.9973 g of Se were weighed to prepare the pristine SnSe. And for the nanocomposite sample a 0.5 wt% of graphene was added. The amounts were weighed in a glove box (mBRAUN) under high purity Argon atmosphere (O_2<0.5 ppm), and sealed in a stainless steel (440c) vial with milling balls of two different sizes (5/16 inches and ¼ inches) at a ball to powder ratio of 10:1. The powder mixture was milled for different milling times of 5, 15, 30 minutes, and 1,2,4,8,12 hours.

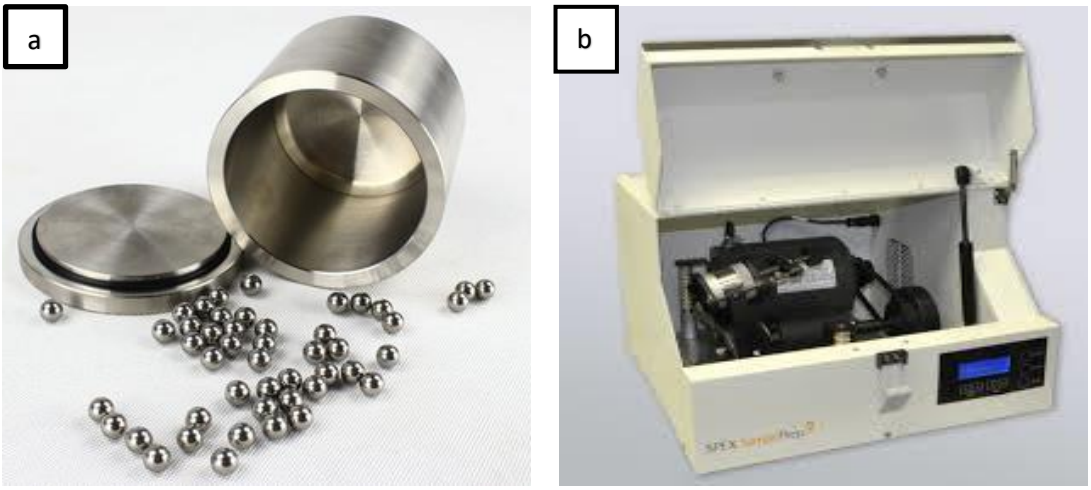

Figure 3.2 a) Stainless steel milling balls and vial, b) SPEX SamplePrep 8000M Mixer/Mil.

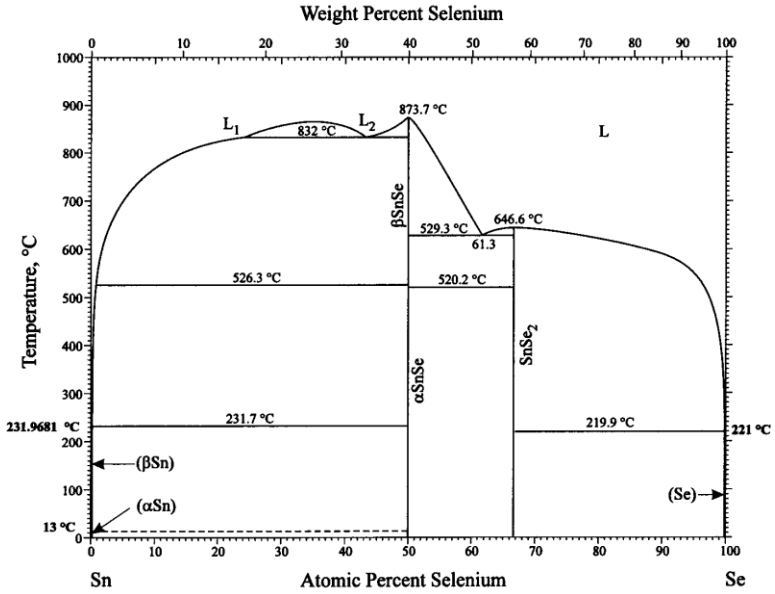

Figure 3.3 SnSe Phase diagram [40].

3.2.2 Spark Plasma Sintering

Spark Plasma Sintering (SPS) is a consolidation technique similar to hot pressing. It is characterized by the high rate of heating by conducting a pulsed direct current through a graphite die while applying hydrostatic uniaxial pressure. It is a very fast process which gives the advantage of preventing grain growth of the nanoparticles and achieving high densification and fewer defects [5][24][95].

In this work, the samples were sent to Fraunhofer Institute for Ceramic Technologies and Systems in Germany for consolidation in a Hybrid-Heated Fast/SPS (HHPD25). Around 9.1 g of sample powder was fed into a cylindrical die lined with graphite sheet, the mold set used is shown in Figure 3.4. This assembly was put into the SPS chamber under vacuum atmosphere, then is was heated at a rate of 100^{o}C/min with

simultaneous application of pressure. The maximum temperature reached was 435ºC and the maximum pressure was 500 MPa. Figure 3.5 shows the graphite sheet used and the 20 mm in diameter compacted sample with the lower and upper punches.

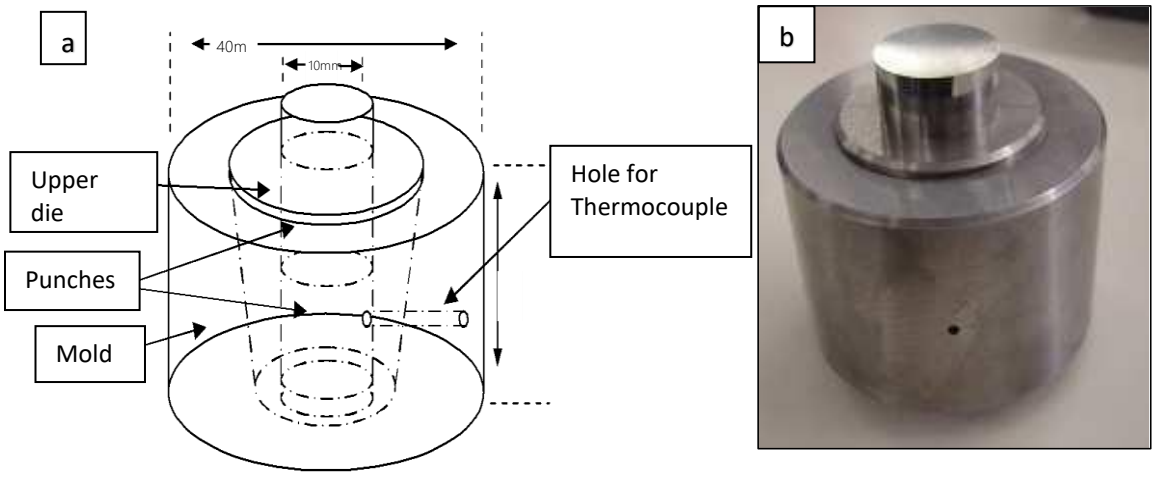

Figure 3.2 a) Schematic diagram of the mold set design, b) The fabricated mold set.

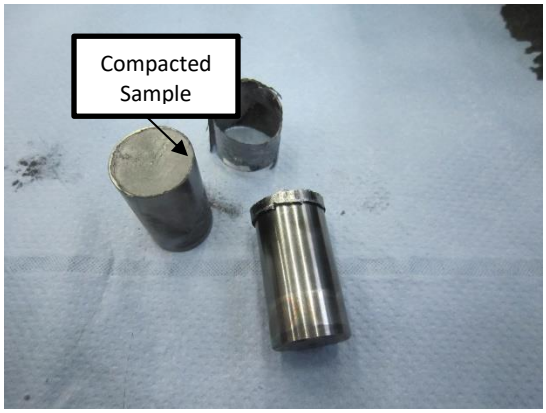

Figure 3.3 Consolidated sample by SPS with the graphite sheet die and the pressing punches.

3.3 Characterization Techniques

3.3.1 X-Ray Diffraction XRD

X-Ray Diffraction (XRD) is one of the most widely used characterization techniques for crystalline matter. It is a non-destructive technique that serves in identifying phases, determining crystal structure and its quality, also it is utilized in lattice parameter measurements, and grain size and strain calculations [96].

The short wavelength of the hard X-rays (i.e. with wavelengths below 0.1-0.2 nm) makes it possible to probe small structures. The crystal structure planes represent a grating that can diffract the incident X-ray beam. Diffraction can only happen if the wavelength of the incident electromagnetic radiation is of the same order as the interatomic distance in the crystal, which should be of the order $1A^{o}$=0.1 nm [96][97]. Bragg explained the occurrence of the characteristic diffraction pattern in 1912 by the constructive interference described in Figure 3.6, and which follows the Bragg's law [97]:

$$n\lambda = 2d_{hkl}sin\theta \tag{3.1}$$

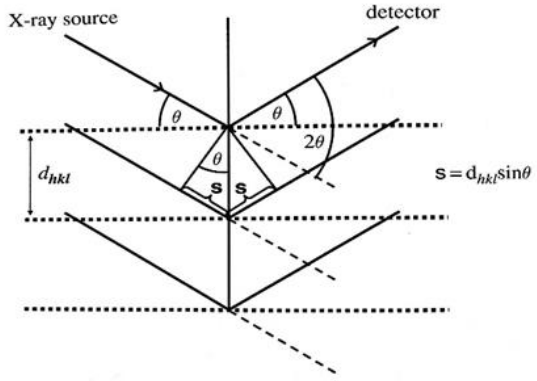

Figure 3.4 Derivation of Bragg's law for a family of (hkl) lattice planes [97].

In this work, powder samples were characterized in a PANalytical Empreon diffractometer system shown in Figure 3.7. The voltage applied was of 45 KV, the target material used was Cu with a wavelength λ=1.54 nm. The measured scattering angle range was 20^o to 100^o at a step size of 0.013 and scan rate of 0.044^o/s.

From the diffraction peaks obtained, the grain size and strain of all sample were calculated using the Averbach method [98]. This method is based on using the Full width at half maxima FWHM of the XRD peak which was obtained from the Gaussian fit of the peaks using OriginPro analysis software. The Averbach formula used was

$$\frac{\beta^2}{tan^2\theta} = \frac{\lambda}{d}\left(\frac{\beta}{tan\theta sin\theta}\right) + 25e^2 \tag{3.2}$$

Where β is the FWHM, θ is the peak's diffraction angle, λ is the X-ray wavelength of 0.154 nm, d is the grain size, and e is the strain.

Figure 3.5 PANalytical Empreon diffractometer system

3.3.2 Transmission Electron Microscopy TEM

Transmission Electron Microscopy TEM is an imaging technique widely used in nanotechnology. It is based on the interaction of an electron beam with an ultrathin sample (less than 100 nm). The De Broglie short wavelength of the electron gives high resolution images that allows the investigation of defects and interfaces at the atomic scale, also provides information about the grain size distribution in the sample. The images produced by TEM comes in in two modes which are the dark field and the bright field. The contrast depends on the thickness and type of material, the heavier the atoms, the stronger the scattering and, as a result, the brighter the signal [99].

TEM was used in this work to measure the grain size and validate the results obtained from XRD of the pristine SnSe and Graphene-SnSe nanocomposite prepared at 4

hours of milling. The powder samples were first compacted into a 3 mm diameter disks by uniaxial cold pressing at 1 GPa pressure in a tungsten carbide mold. Then the samples were prepared by Focused Ion Beam (FIB) methodology[100] using a FEI Quanta 3D field emission gun on a Dual Beam instrument. The disks were thinned first by mechanical dimpling to around 200 nm to reduce the ion beam thinning time, then placed into the FBI in which Argon ions bombard the sample and sputtering takes place until the material becomes electron transparent. These preparation steps are shown in Figure 3.8. A JEOL 2000FX Scanning Transmission Electron Microscope (STEM) operated at 200 Kv, shown in Figure 3.9, was used to obtain the dark field and bright field images for the samples.

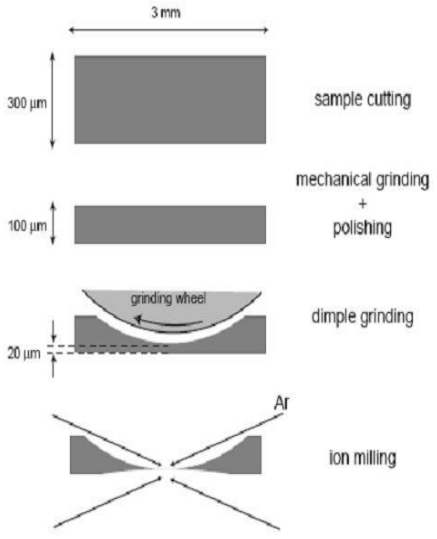

Figure 3.6 Sample preparation steps for TEM by ion milling technique.

Figure 3.7 FIB FEI Quanta 3D field emission gun.

3.3.3 Scanning Tunneling Electron Microscopy (STEM)

Scanning Tunneling Electron Microscopy (STEM) is a high-resolution imaging technique used to characterize the nanoscale and atomic scale structures of the material. In this technique the electron beam is focused to a fine spot where each point is parallel to the optical axis. There are two imaging modes: High-Annular Angle Dark Field (HAADF) and Bright Field (BF). In HAADF mode, the images are formed by the incident scattered electrons from the annular detector. The high-resolution images obtained from this mode are directly related to the atomic number of the elements, this imaging is called the Z-contrast [101].

STEM was used in this work to study the elements distribution and Graphene position in the nanocomposite sample. The Graphene-SnSe composite powder sample prepared at 4 hours of milling was compacted into a 3 mm in diameter disc by uniaxial

cold pressing at 1 GPa pressure in a tungsten carbide mold. The sample was then prepared by focused Ion Beam methodology using a FEI Helios NanoLab G4 with 30 kV Gallium ions, it was followed by a 1-5 kV milling to minimize damaged surface layers. FEI Titan G2 60-300 STEM operated at 200 keV was used for the characterization in this work. The Convergence semi angle was 24 mrad, the High-angle annular dark-field (HAADF) detector angles were at 50-200 mrad. And for the EDX mapping, the screen current was at 150-200 pA.

3.3.4 Differential scanning calorimetry DSC

Differential scanning calorimetry (DSC) provides information about the phase changes exhibited by a sample such as the thermal critical points like melting point, enthalpy, specific heat or glass transition and crystallinity which is determined by measuring the heat associated with fusion of polymer. This technique consists of measuring the heat flow difference as a function of time between a sample and a reference which has a well-defined heat capacity [102]. Differential Scanning Calorimetry (DSC 8500 Perkin Elmer), shown in Figure 3.10, was used to investigate the phases changes and grain growth of the SnSe sample to determine the suitable temperature for SPS. The temperature range was from room temperature to 550 ^{o}C at a rate of 10^{o}C/min.

Figure 3.8 Differential Scanning Calorimetry (DSC 8500 Perkin Elmer).

3.3.5 Vickers micro-hardness test

Vickers micro-hardness is a non-destructive characterization technique to evaluate the mechanical properties of a sample. The hardness values obtained from this test reflect the resistance of the material to localized plastic deformation. For small particles samples Vickers Micro-Indentation provide a symmetrical configuration that is most suitable for small particles at very small loads [103]

All the samples at different milling times were compacted into 10 mm disks by uniaxial cold pressing at 2GPa pressure in a tungsten carbide mold. Vickers micro-hardness tester FM ARS 9000, shown in Figure 3.11, was used to measure the hardness. The test was carried out under a 10-gf diamond indenter load. Five indentations were made along the surface of the sample and the indents diagonals were measured by using the microscope to obtain the HV hardness value.

Figure 3.9 Vickers micro-hardness tester FM ARS 9000.

3.3.6 Thermoelectric properties characterization

The samples prepared by SPS were used for thermoelectric properties characterization. Seebeck coefficient and electrical conductivity were both measured simultaneously in SBA 458 Nemesis system, shown in Figure 3.12, at 100^{o}C, 300 ^{o}C, 500 ^{o}C, and 600 ^{o}C. The setup shown in Figure 3.13 used the 4-point method for measurement. Current pins and thermocouples are placed on the lower surface of the sample. At the two bottom edges micro heaters are placed to create temperature gradient in both directions, and the developed voltage is measured by the thermocouple wires. For electrical conductivity measurement, different current values were applied and the resulting voltage was measured. And by simple division of voltage by electrical current, the electrical resistivity value is obtained. The relation between the resulting voltage and the temperature gradient gives the Seebeck coefficient value.

$$S = \frac{\Delta V}{\Delta T} \tag{3.3}$$

Figure 3.10 SBA 458 Nemesis system.

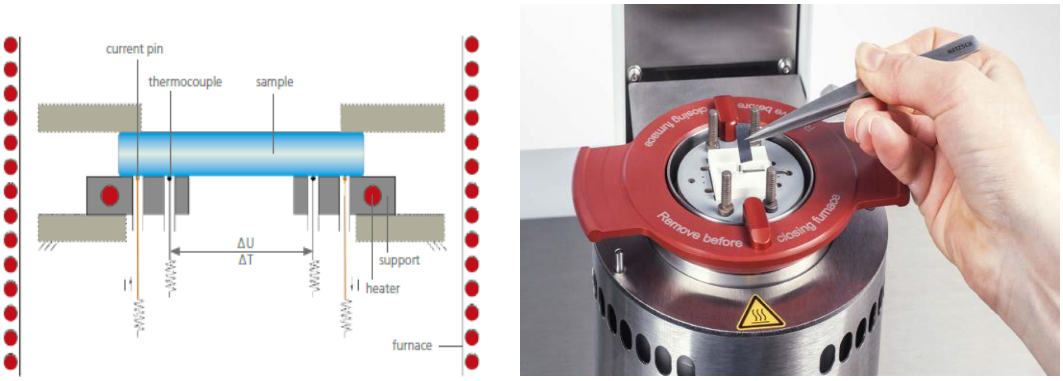

Figure 3.11 Measurement setup of the SBA 458 Nemesis for the temperature range between RT and 800°C.

To determine thermal conductivity, Light Flash Apparatus LFA 467 HyperFlash as shown in Figure 3.14, was used. The light flash technique is a fast, non-destructive, non-contact method used to determine thermophysical properties. The sample front surface is heated by a short energy light pulse. An infrared detector (IR), at the back surface of the sample, measures the resulting temperature excursion from which thermal diffusivity and specific heat are determined. Thermal conductivity can thus be calculated from the equation

$$\lambda(T) = a(T) \cdot C_P(T) \cdot \rho(T) \quad (3.4)$$

Where λ is the thermal conductivity [W/(m·K)], a is thermal diffusivity [mm²/s], Cp is the specific heat [J/(g·K)], and ρ is bulk density [g/cm^3]. Figure 3.15 the measuring setup.

Figure 3.12 Light Flash Apparatus LFA 467 HyperFlash.

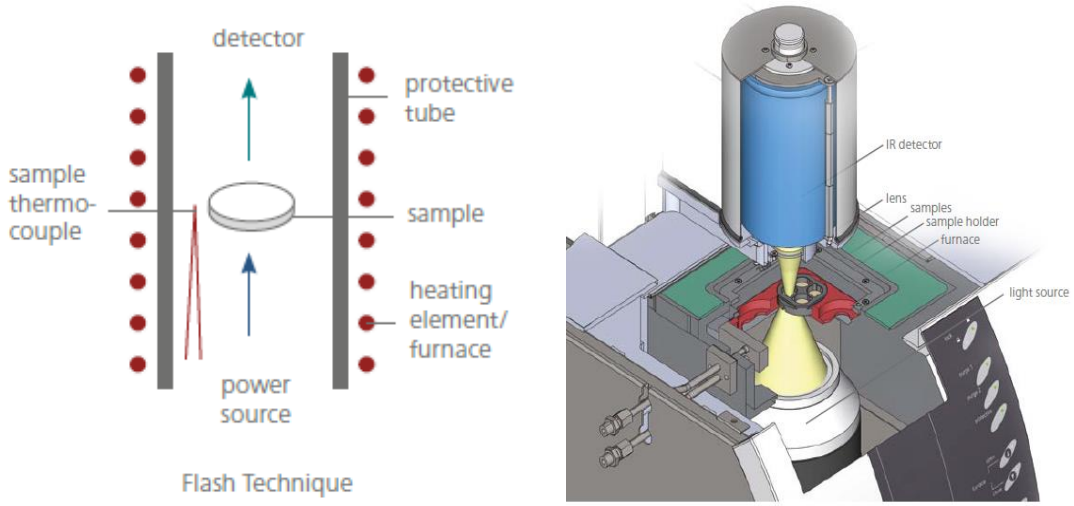

Figure 3.13 Measurement setup of Light Flash Apparatus

CHAPTER 4: RESULTS AND DISCUSSION

4.1 Structural Characterization

4.1.1 X-Ray Diffraction analysis

Figure 4.1 exhibits the XRD patterns of the prepared SnSe at different milling times. The evolution of the peaks and the formation of the intermetallic compound is clear with increasing milling time. Starting from 1 hour of milling, the patterns show the disappearance of Sn and Se separate elements and the formation of SnSe intermetallic compound phase. For longer times of milling the characteristic peaks are consistent with the standard peaks of orthorhombic SnSe (JCPDS No. 48-1224). The diffraction patterns show an increase in peak broadening, which indicates a refinement in grain size with increasing milling time. This was further analyzed by estimating the grain size and strain using the Averbach method that considers the FWHM of the peaks as explained in chapter 3 section 3.2.1. The Averbach formula is

$$\frac{\beta^2}{tan^2\theta} = \frac{\lambda}{d}\left(\frac{\beta}{tan\theta sin\theta}\right) + 25e^2 \qquad (4.1)$$

Figure 4.2 shows an example of the linear fit of $\frac{\beta^2}{tan^2\theta}$ versus $\frac{\beta}{tan\theta sin\theta}$ for the measured peaks at 2 hours of milling, the slope and the intercept were used to calculate the grain size and strain. Figure 3.4 shows the variation of grain size and strain with milling time for all samples. It is noted from Figure 4.3 that grain size decreased gradually with milling time and reached to a value of 11 nm after 4 hours of milling. No further decrease was observed beyond 4 hours, see Figure 4.3. The lattice strain decreased with milling time and reached a value of 0.283 % after 1 hour of milling. A further decrease was

observed after 8 hours of milling as shown in Figure 4.3. According to this finding, we adapted the 4 hours to be the maximum milling time on the studied material.

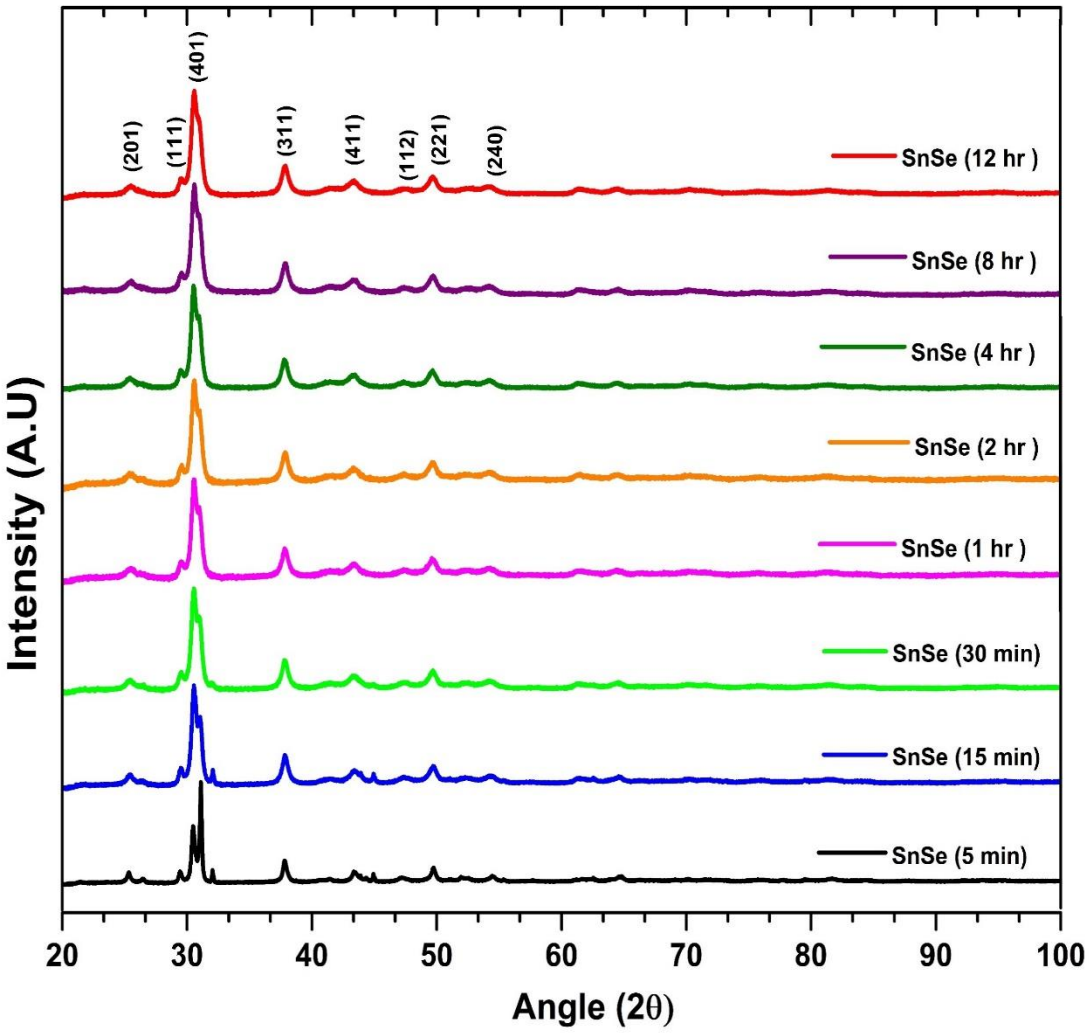

Figure 4.1 XRD patterns of SnSe at different milling times.

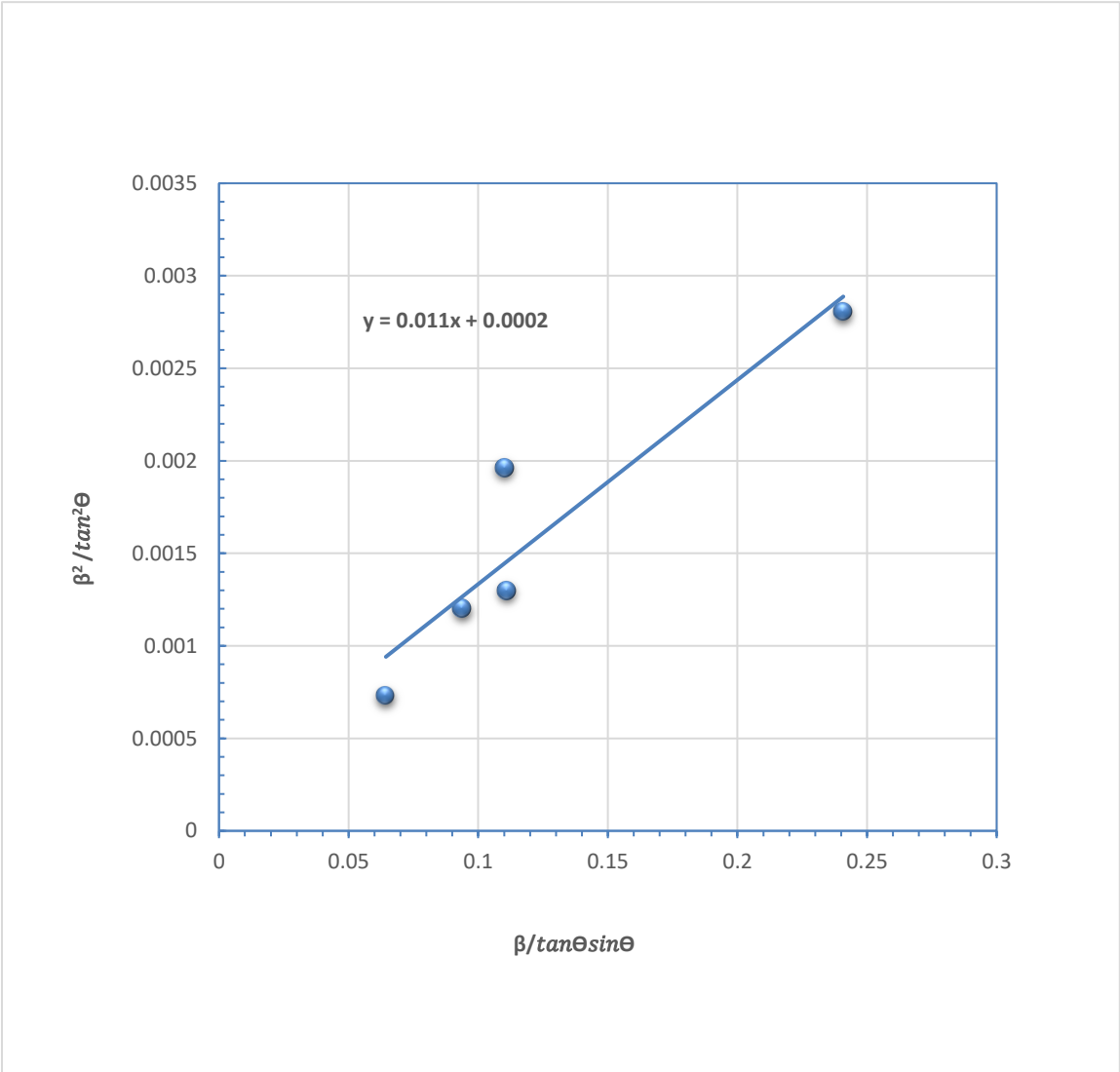

Figure 4.2 Linear fit of Averbach method for sample prepared at 2 hours of milling.

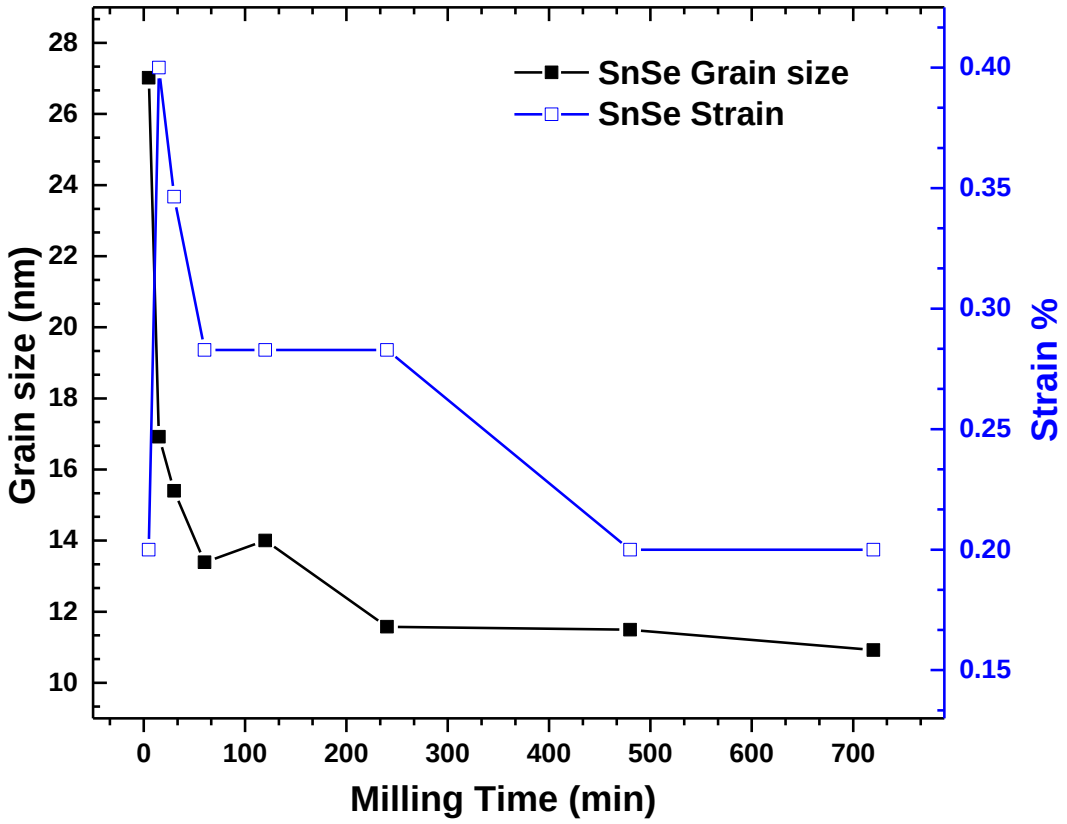

Figure 4.3 Grain size and Lattice strain of SnSe as function of milling time.

Figure 4.4 shows the XRD patterns of the Graphene-SnSe composite. The evolution of peaks shows a similar behavior as the one described for the pristine SnSe, and there is no shift or additional peaks observed which is expected, as only a small amount of 0.5 wt% of Graphene was added. The absence of graphene diffraction peaks was also reported when Graphene was added to Bismuth Telluride Bi_2Te_3 [87][91]. The Averbach method was used to estimate the grain size and strain of the prepared nanocomposites. Figure 4.5 shows

the calculated grain size and lattice strain of SnSe-Graphene as a function of milling time. After 30 minutes of milling, only a small change in grain size and strain is observed for longer times of milling, however at 4 hours there is further decrease in grain size accompanied by an increase in strain, which may be caused by the presence of defects at the grain boundaries that create an excess volume which induces short-range stress field, this is the dominant factor leading to the lattice strain in nanocrystalline materials [104]. These results are in agreement to the results obtained for the pristine SnSe and it indicates that Graphene-SnSe nanocomposite was successfully synthesized at 4 hours of milling with an average grain size of about 8 nm and strain of 0.346%.

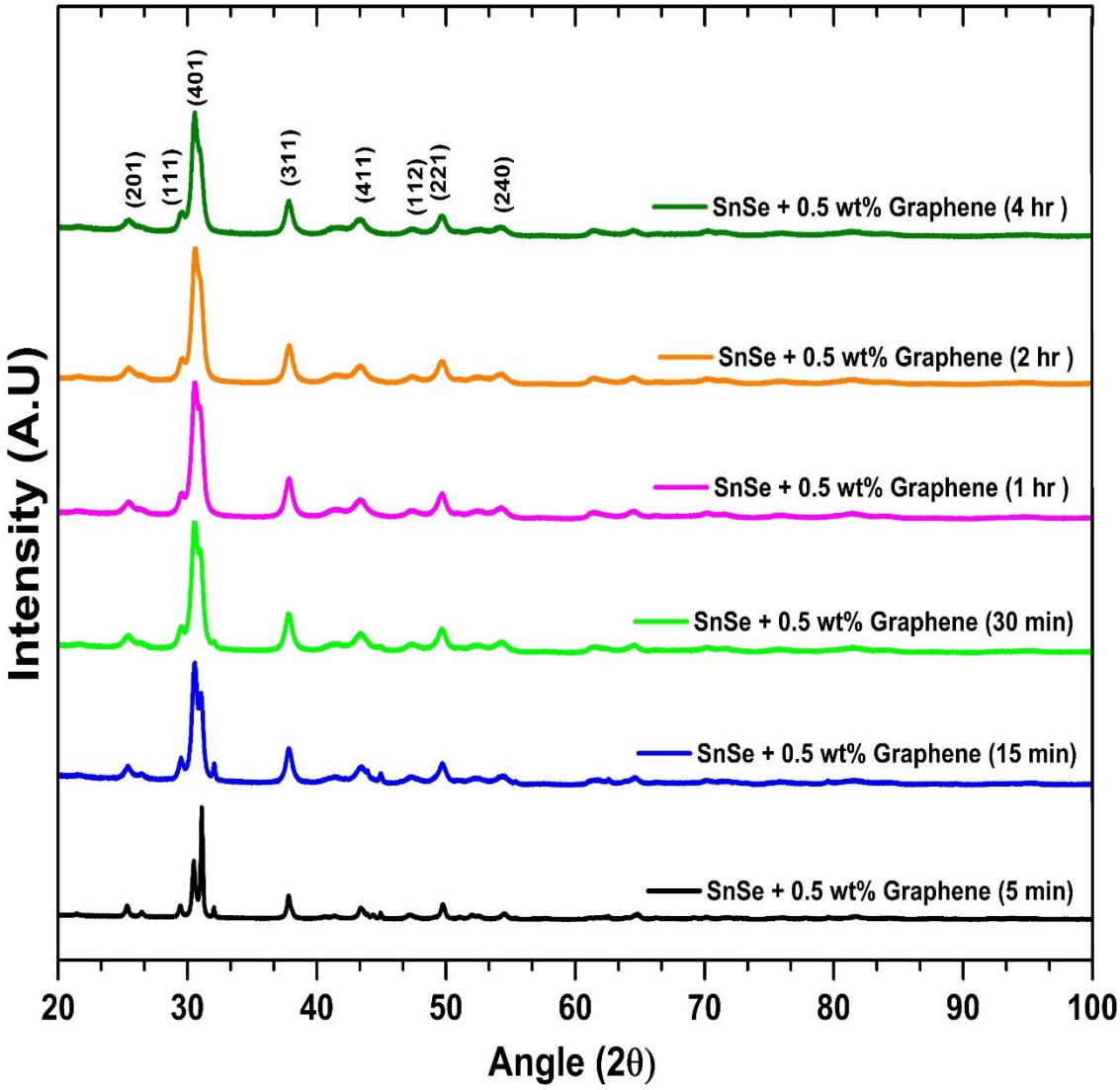

Figure 4.4 XRD patterns of Graphene-SnSe at different milling times

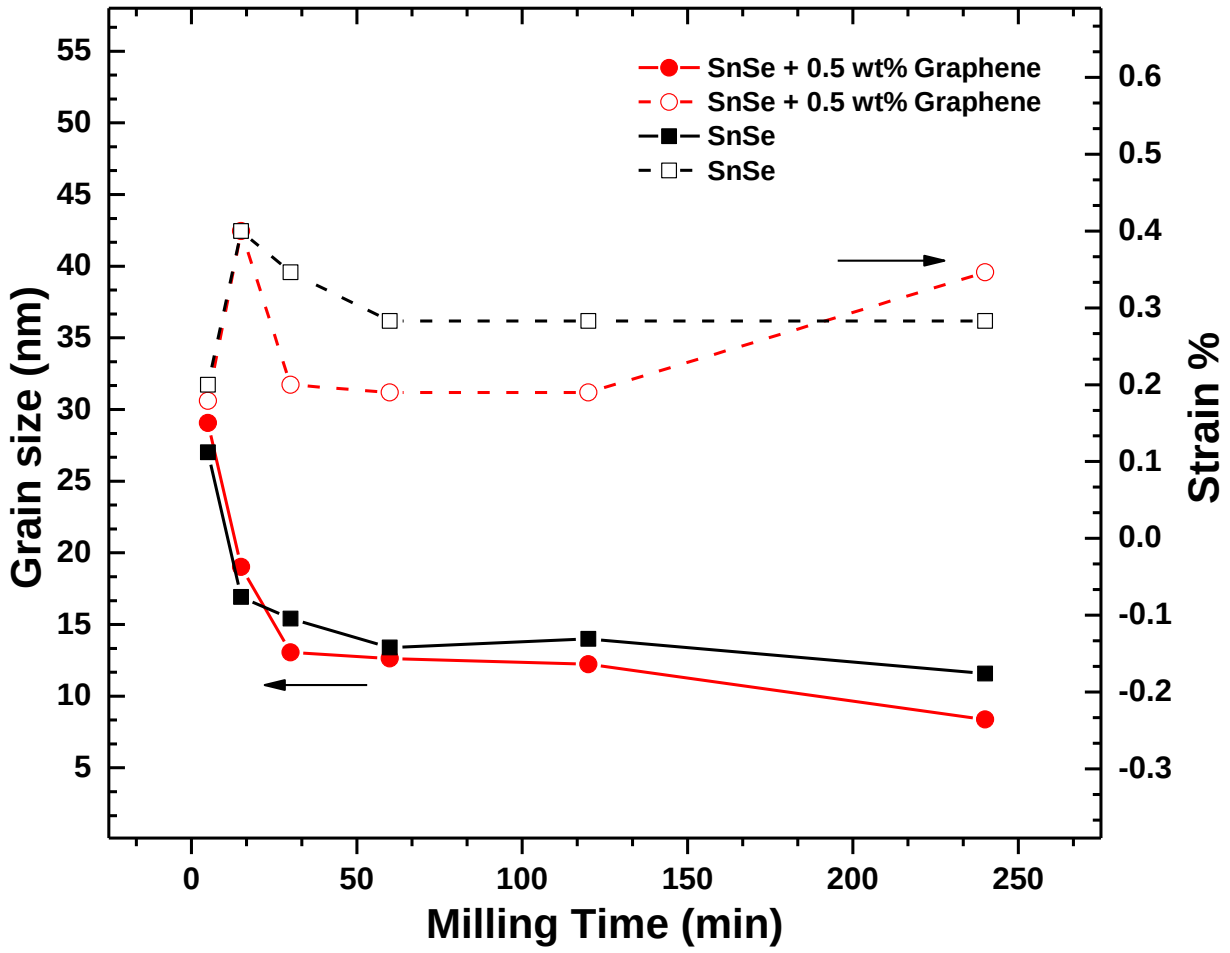

Figure 4.5 Grain size and Strain of pristine SnSe and Graphene-SnSe nanocomposite as function of milling time.

4.1.2 Transmission Electron Microscopy of pristine SnSe and SnSe nanocomposite

For further investigation of structure and grain size, TEM was performed on the pristine SnSe and the Graphene-SnSe nanocomposite prepared at 4 hours of milling time. Figure 4.6 and Figure 4.7 show the bright-field and dark-field TEM image of SnSe and Graphene-SnSe respectively. It can be seen from the bright-field images that the nano grains are equiaxed with high angle grain boundaries. Dark field images were used to calculate the average grain size. Figure 4.6.c and Figure 4.7.c show the statistical distribution of the grain size for both samples. For the pristine SnSe a total of 165 grains were measured and the average grain size was found to be 10 nm, with an upper limit of grain size distribution of 25 nm. For the nanocomposite an average grain size of 11 nm was obtained from the 525 grains measured with very narrow grain size distribution. These results are consistent with the grain size value obtained from the XRD analysis and small differences might be due to the fitting of the Averbach method or the non-perfect circularity of the grains appearing in the TEM images. These results confirm the success of the nano-structuring of SnSe by using the high energy ball milling technique. Shuai Lv et al. [105] prepared polycrystalline SnSe by mechanical alloying using a planetary ball mill and obtained a grain size ranging from 100 nm to 300 nm. The smaller grain size obtained in our study could be related to the higher energy of the SPEX ball milling in comparison to the planetary ball milling. Tyagi et al. [38] used vacuum melting technique and reached a grain size between 40 to 50 nm. Sanchez et al. [42] were able to obtain a fine nanostructure of SnSe platelets with layers thickness ranging from 15 to 30 nm by using the arc melting technique.

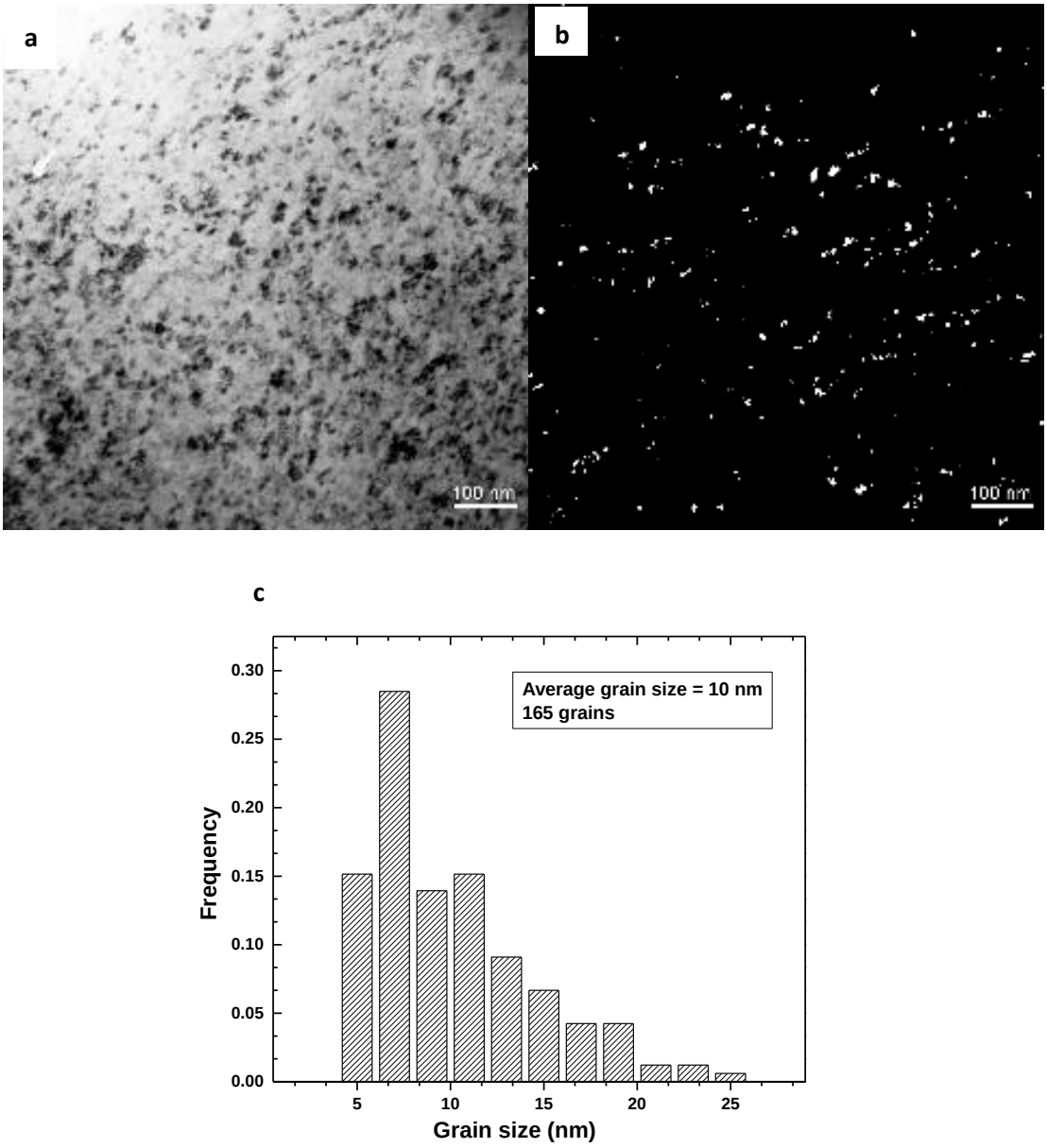

Figure 4.6 a) A bright-field TEM image, b) A dark-field TEM image, c) Grain size distribution of pristine SnSe prepared at 4 hours milling.

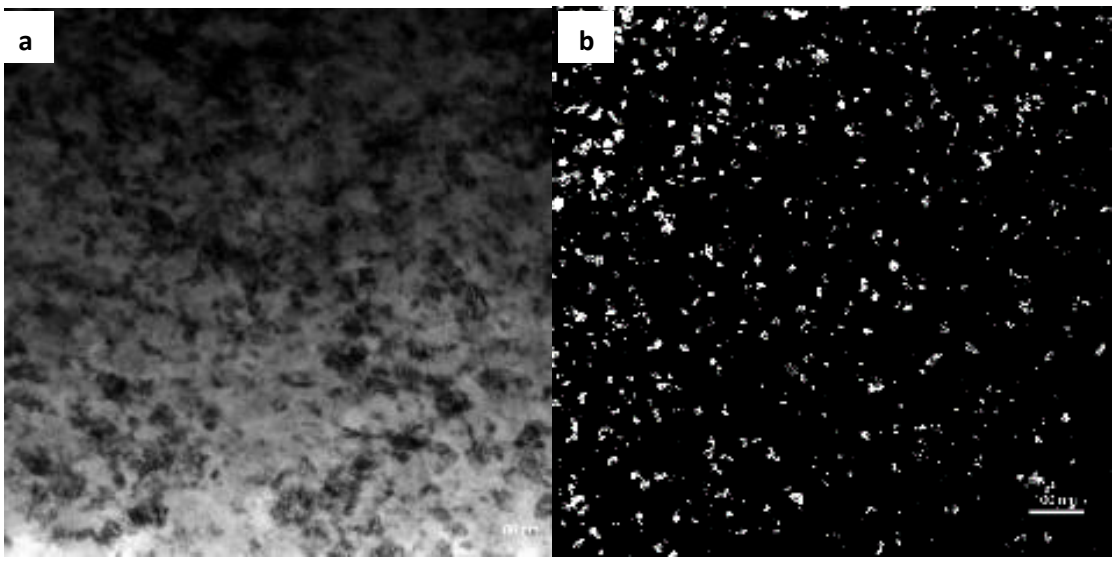

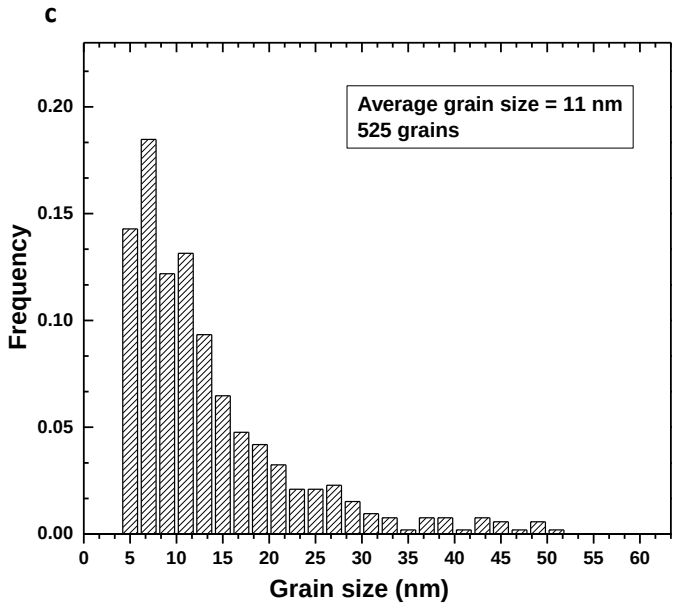

Figure 4.7 a) A bright-field TEM image, b) A dark-field TEM image, c) Grain size distribution of Graphene-SnSe nanocomposite prepared at 4 hours milling.

4.2 Hardness Characterization of pristine and SnSe nanocomposite

The selection of good thermoelectric materials is not only related to the high ZT value, but it is also highly dependent on the mechanical properties of the material. Thermoelectric devices are exposed to thermal and mechanical stresses, therefore, good mechanical properties are critical design criteria [106].

Vickers microhardness test was performed on all prepared samples of the pristine SnSe and Graphene-SnSe nanocomposites. The hardness values with respect to milling time are presented in Figure 4.8. It can be seen that in both materials, hardness increased gradually with milling time and reached to a maximum value and a plateau trend after 2 hours of milling time. It is shown that all the prepared samples have high hardness values, more than 0.27 GPa obtained by Tyagi et al. [38], and it increases with increasing the milling time. This behavior is due to the strong nanostructuring, since grain refinement is a strengthening mechanism in which grain boundaries act as barriers to prevent dislocation motion. After around 2 hours of milling the hardness values are almost constant, this comes in agreement with the XRD results showing that the slight change in grain size after 2 hours of milling. The hardness of the Graphene-SnSe nanocomposites is less than the pristine SnSe, this softening can be explained by the sliding at the grain boundaries that happen at very small grain sizes of less than 20 nm. At this small scale, the deformation is governed by the large fraction of atoms at grain boundaries [107] [108]. At 4 hours of milling the hardness value of pristine SnSe is 1.725±0.002 GPa, and for the Graphene-SnSe nanocomposite it is 1.496±0.051 GPa. These hardness values are considered to be the highest reported for this structure so far.

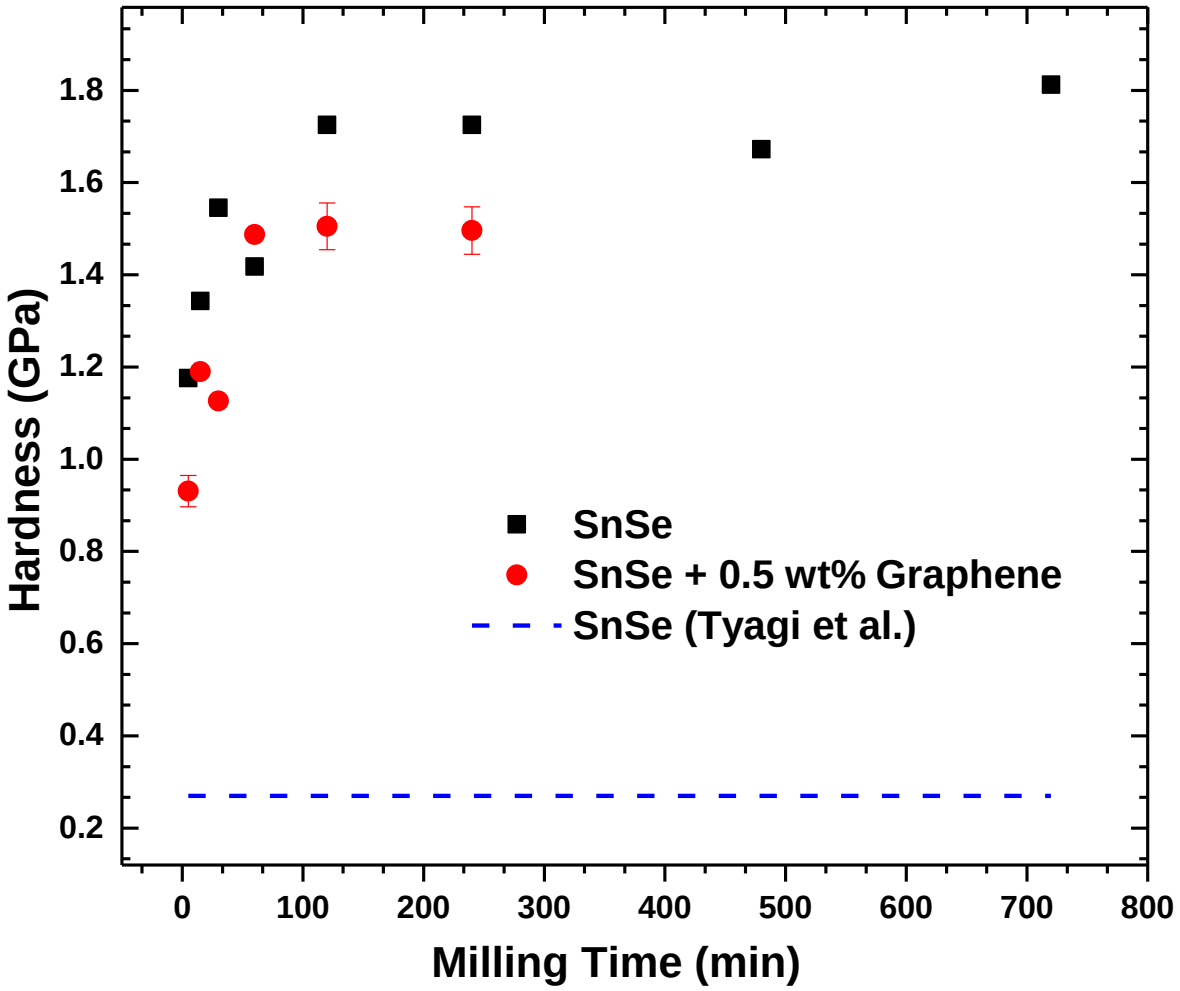

Figure 4.8 Hardness values as function of milling time of pristine SnSe and Graphene-SnSe nanocomposite.

4.3 Thermal behavior of pristine SnSe

In order to investigate the possibility of grain growth and to identify the consolidation temperature of the milled powder, the stability and the thermal behavior of the prepared samples was investigated by DSC analysis. A Heating followed by cooling cycle was

performed on the pristine SnSe and no peak was observed from RT to 550^{o}C as shown in Figure 4.9. This indicates that no phase transition or grain growth occured in this temperature range. In fact, Sanchez et al. [41] performed DSC analysis on polycrystalline SnSe and the measurements suggested a transition occurring at 750 ^{o}C. These results confirm the possibility of performing SPS at lower temperature than 750 ^{o}C for samples consolidation without significant grain growth.

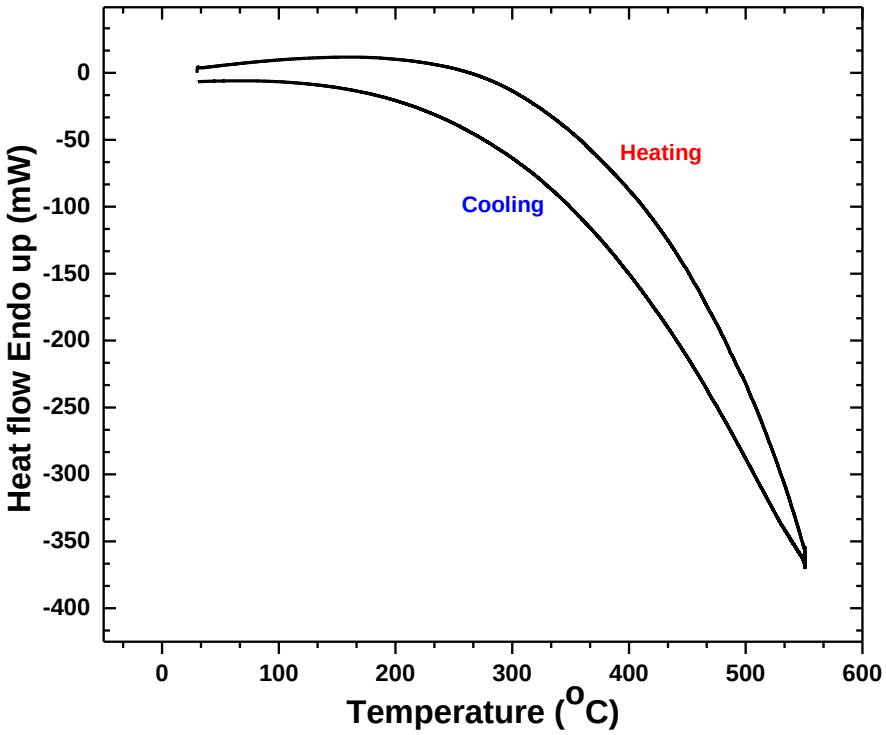

Figure 4.9 DSC curve of pristine SnSe prepared at 4 hours of milling.

4.4 Thermoelectric transport measurements

The temperature dependence of Electrical resistivity ρ, Seebeck coefficient S, Power factor PF, and Thermal conductivity κ are presented in Figure 4.10 for both samples pristine SnSe and Graphene-SnSe nanocomposite, prepared at 4 hours of milling and consolidated by SPS.

4.4.1 Thermoelectric properties of pristine SnSe

Figure 4.10.a shows the variation of electrical resistivity of both SnSe and Graphene-SnSe samples as a function of temperature. It can be seen that there is a decrease in resistivity with increasing temperature which is consistent with a semiconductor behavior, where the increase in temperature increases the number of free charge carriers therefore increases the conductivity according to the equation

$$\sigma = nq\mu \tag{4.2}$$

where σ is conductivity, n is the charge carriers number, q is the charge, and μ is the mobility. However, the resistivity increased after 773 K, this can be explained by the increase of charge carrier scattering at high temperatures and the high density of grain boundaries acting as barriers due to the strong nanostructuring. For the pristine SnSe the resistivity decreases from 2.52 mΩ.m at 373 K to 1.53 mΩ.m at 773 K, then it increases to 2.1 mΩ.m. These values are lower than the ones obtained from previous studies conducted on SnSe. The electrical resistivity of single crystal SnSe prepared by Zhao et al. is in the range of 5 mΩ.m to 10 mΩ.m in the a-direction at the temperature range from 300 to 400 K. while Sassi et al. reported a value around 11 mΩ.m between 300 and 400 K.

The change in Seebeck coefficient with temperature is presented in figure 4.10.b.

This figure shows a gradual increase of Seebeck coefficient with increasing temperature. The increment of Seebeck coefficient with increasing temperature despite the increase in electrical conductivity can be often noticed in some thermoelectric materials. The nanostructured SnSe prepared by Sanchez et al. [42] exhibited similar behavior and the authors explained this behavior by the strong nanostructuring of the samples that caused the formation of more grain boundaries that act as scattering barriers for the charge carriers. Chen et al.[66] attributed this behavior in their Ag doped samples to the presence of deep level defects that increases the scattering factor. However, at the higher temperature of 873 K, the Seebeck coefficient increase with the decrease in conductivity. This behavior is observed in many studies on thermoelectric SnSe. In fact, the Seebeck coefficient is related to both carrier concentration and the scattering factor by the equation [60]

$$S = \frac{k_B}{k_B(\gamma + C - ln\, n)} \tag{4.3}$$

where k_B is the Boltzmann constant, γ is the scattering factor, C is a material constant, and n is the carrier concentration. Very high Seebeck coefficients where attained from this work, a high value of 723 µV/K at 373 was reached for pristine SnSe and it increased to 1032 µV/K at 873K. These values are the highest so far for SnSe according to the literature, Sanchez et al. [42] attained a value of 668 µV/K at 380 K, and Popuri et al. [57] reported a Seebeck coefficient of 525 µV/K at 873K.

The relation between the resistivity and Seebeck coefficient is expressed by the power factor as

$$\mathrm{PF} = \frac{S^2}{\rho} \tag{4.4}$$

The power factor is presented in Figure 4.10.c as function of temperature. The PF increases with increasing temperature, and it slightly decreases at 873 K for pristine SnSe due to the increase of electrical resistivity observed at the same temperature. The PF has a highest value of 527 $\mu W/mK^2$ at 773 K for the pristine SnSe.

The dependence of thermal conductivity on temperature is presented in Figure 4.10.d. A decrease in κ is observed with increasing temperature. For pristine SnSe, thermal conductivity has a value of 0.7 W/m.K at 373 K, and it decreases to reach around 0.5 W/m.K at 873 K. These values are considered high compared to the ones obtained in literature for polycrystalline SnSe, Sanchez et al. [42] were able to reach an extremely low thermal conductivity of less than 0.1 W/m.K around room temperature.

4.4.2 Thermoelectric properties of Graphene-SnSe nanocomposite

To further enhance the thermoelectric properties of the nanostructured SnSe, 0.5 wt% of Graphene was added. From Figure 4.10.a, the temperature dependence of electrical resistivity of the graphene-SnSe nanocomposite is similar to the pristine SnSe. The enhancement in conductivity is noted as the nanocomposite sample exhibits lower resistivity due to the presence of graphene which increases the charge density and provide extra transmission channels for the electrons. The resistivity decreases from 2.13 mΩ.m at 373 K to 1.07 mΩ.m at 773 K, then it increases to 1.4 mΩ.m at 873 K.

The Seebeck coefficient presented in Figure 4.10.b shows the same trend as the pristine SnSe. However, the values are slightly lower due to the increase in the charge concentration upon the addition of graphene. At 873 K, the Seebeck coefficient of the nanocomposite is larger than the pristine SnSe and reaches a high value of 1140 µV/K.

This increase corresponds to the decrease in electrical conductivity at this high temperature causing the decrease in mobility as well as the presence of extra scattering boundaries created by the addition of graphene.

The power factor of the SnSe nanocomposite is higher than the pristine SnSe due to lower electrical resistivity at the whole temperature range. PF keeps increasing with temperature as shown in Figure 4.10.b. The highest value of 896 $\mu W/mK^2$ was reached at 873 K, and it is of 243 $\mu W/mK^2$ at 373 K. The power factor of Bi_2Te_3/Graphene composite prepared by Ju et al. [92] reached a high of 700 $\mu W/mK^2$ at 300 K with the same Graphene content of 0.5 wt%.

The thermal conductivity of Graphene-SnSe nanocomposite is much lower than the pure SnSe. This can be explained by the role of Graphene in creating extra phonon scattering centers by forming heterointerfaces and defects. The thermal conductivity reaches a low value of 0.4 at 773 K, however, it increases to around 0.6 at 873 K.

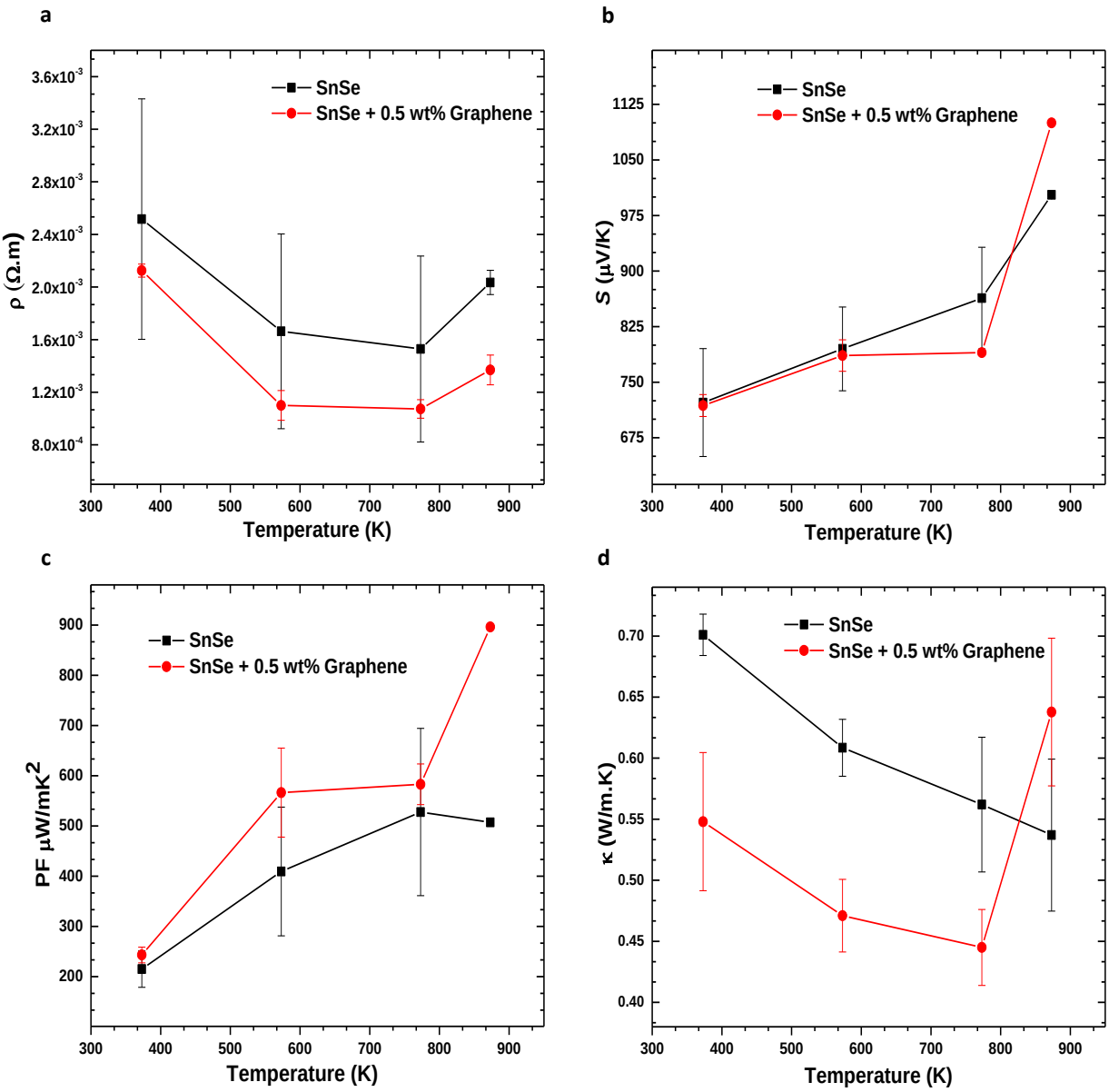

Figure 4.10 Temperature dependence of a) Electrical resistivity, b) Seebeck coefficient, c) Thermal conductivity, d) Power factor for SnSe and SnSe-Graphene nanocomposite.

4.4.3 Figure of merit pristine SnSe and SnSe nanocomposite

Figure *4.11* presents the figure of merit for the prepared nanostructured SnSe and Graphene-SnSe nanocomposite in comparison with ZT values of previous studies on SnSe. The ZT value of the pristine SnSe increase from 0.1 at 373 K to 0.9 at 873 K, this enhancement compared to the previous reports is due to the strong nanostructuring effect. And for the nanocomposite the ZT reaches a high value of 1.2 at 873 K. This enhanced ZT is due to the higher power factor upon the addition of graphene. The results obtained from this work are very promising since further improvement of efficiency can be expected with doping.

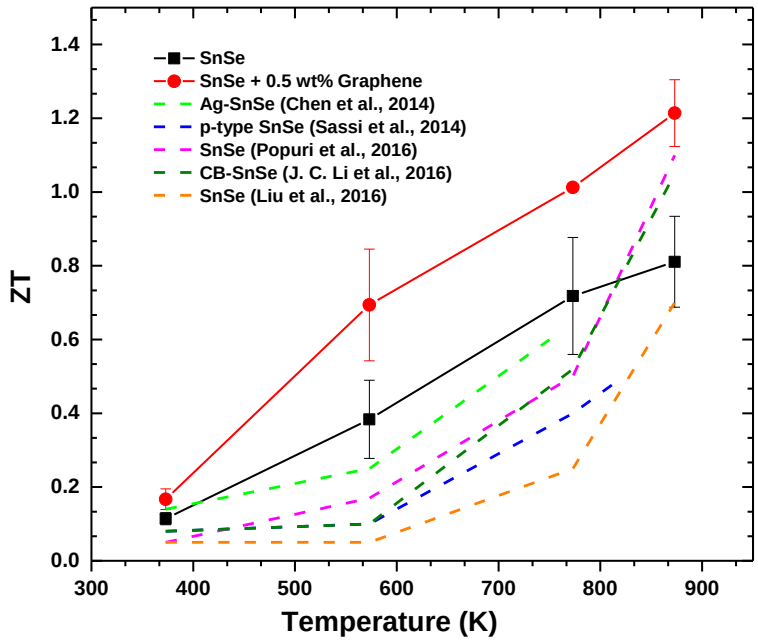

Figure 4.11 Comparison of figure of merit ZT between the prepared pristine SnSe and Graphene-SnSe nanocomposite and previous studies.

4.5 Scanning Tunneling Electron Microscopy of Graphene-SnSe nanocomposite

To prove the effect of the Graphene and explain the enhancement of the thermoelectric performance. A scanning tunneling electron microscopy was conducted on the composite sample to study the elements present and show the exact position of graphene in the material. Figure 4.12.a shows the grains distributed in the sample and Figure 4.12.b shows at a higher magnification of the grain boundaries with the presence of some voids due to compacting conditions conducted on the sample.

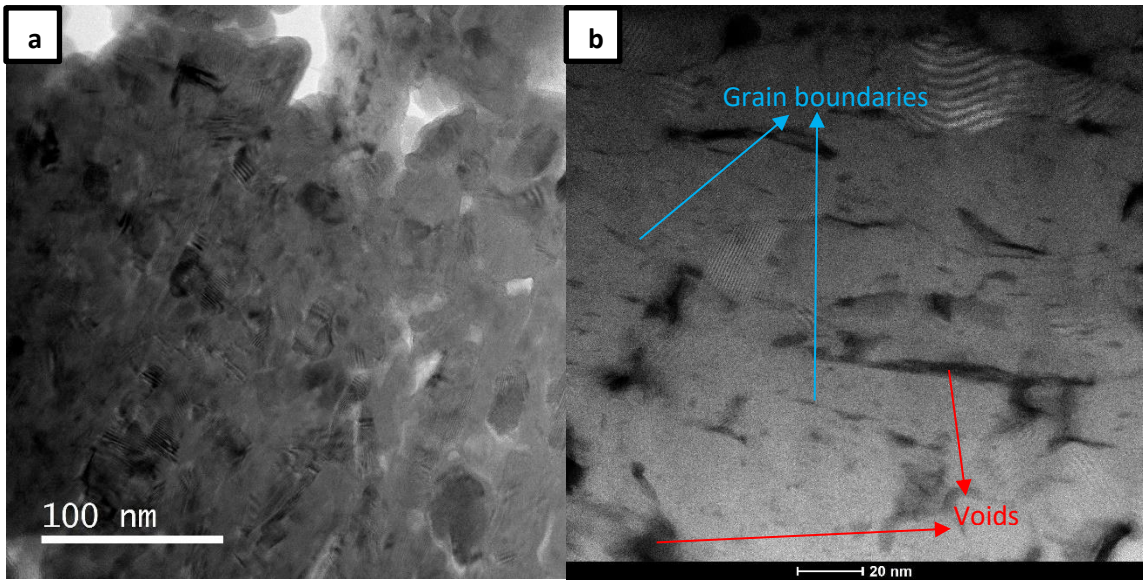

Figure 4.12 STEM Bright Field images of Graphene-SnSe nanocomposite sample.

Figure 4.13 presents the bright field and high-angle annular dark field images of the grain boundary at high magnifications. The images show the presence of some lines in a layered structure at the boundary. The calculated spacing between these layers is about 0.65 nm which is similar to the graphite double interlayer spacing.

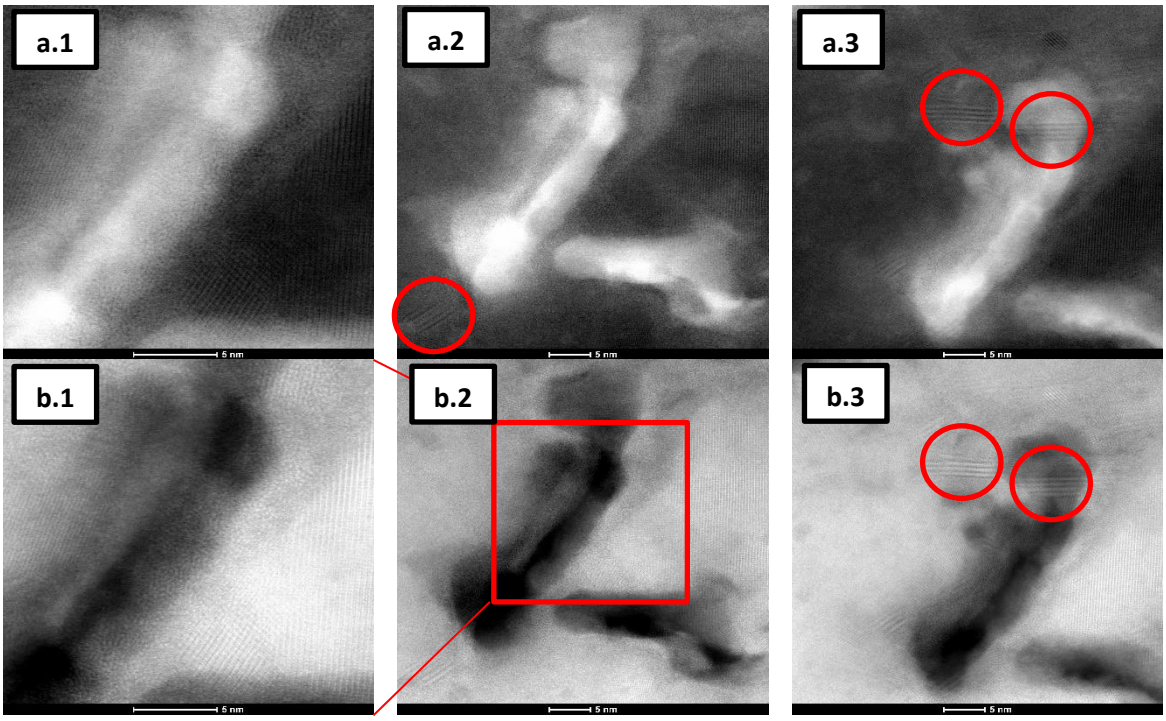

Figure 4.13 a) Bright field images, b) HAADF images of Graphene-SnSe nanocomposite at different magnifications.

Energy Dispersive X-ray (EDX) mapping was performed to confirm the elements present in the composite sample and their distribution. A uniform even distribution all over the sample is observed for both Selenium and Tin elements as shown in Figures 4.14.b and 4.14.c respectively, with some dark spots representing the grain boundaries. The Oxygen distribution is shown in Figure 4.14.d, the presence of oxygen in the sample might be due to the analysis conditions and environment. In Figure 4.14.e, the red color represents the carbon signals, which reveals that graphene is segregated around the boundaries. This observation is further confirmed by the overlaid map in Figure 4.14.f. Higher magnification images of the grain boundary are presented in Figure 4.15. This mapping confirms the segregation of graphene at the grain boundary by the high intensity carbon signals in Figure 4.15.e and in Figure 4.15.f that shows the overlaid mapping of all elements.

This is the first ever reported evidence to identify the location of graphene in a nanocrystalline thermoelectric material. And the results confirm the presence of Graphene at the grain boundaries which acts as an electron transport channel that explains the enhanced electrical conductivity and the high Seebeck coefficient. The Graphene at the boundaries acts as an additional scattering center for the phonons, which is an explanation for the lower thermal conductivity obtained in the thermoelectric results. In addition, at this location, graphene acts as a softening agent giving lower hardness values.

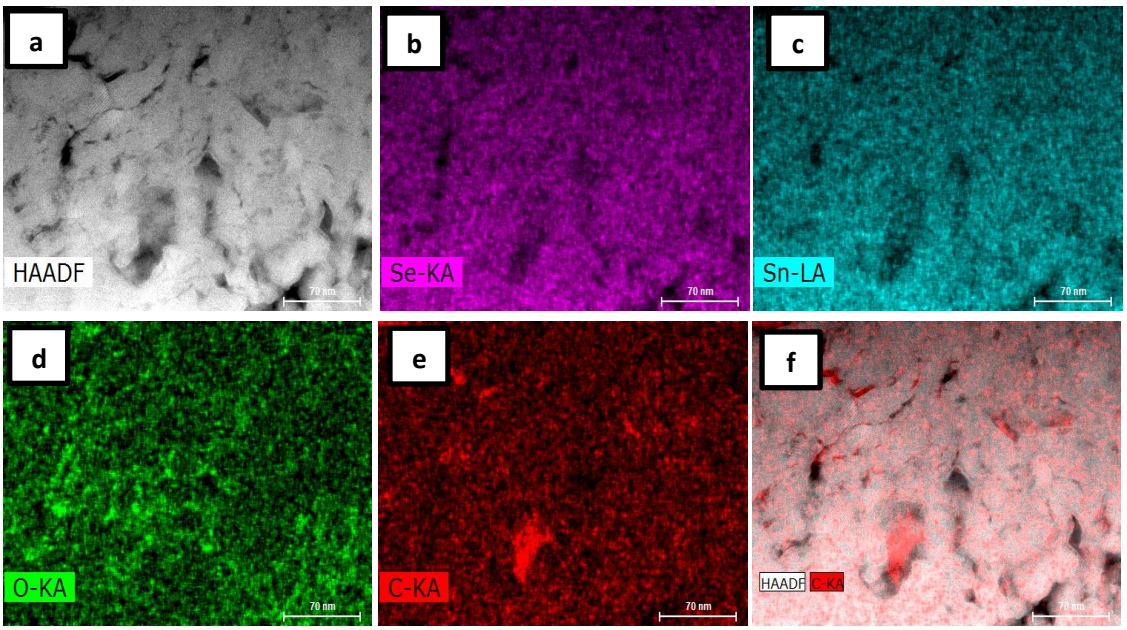

Figure 4.14 EDX mapping for Graphene-SnSe nanocomposite HAAFD images.

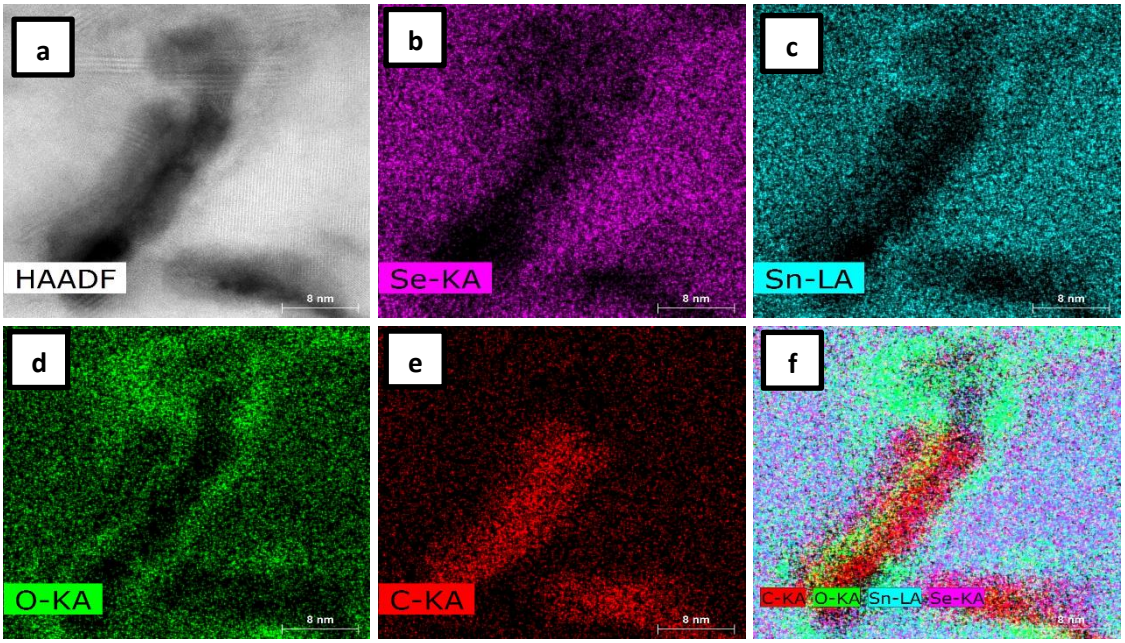

Figure 4.15 EDX mapping for Graphene-SnSe nanocomposite HAAFD images at high magnification.

CHAPTER 5: CONCLUSION

In summary, nanocrystalline SnSe composites were successfully prepared by high energy ball milling under Argon atmosphere. The produced powder was consolidated using Spark Plasma Sintering SPS at maximum temperature of 435^{o}C and pressure of 500 MPa. The structural, mechanical, and thermal properties of the samples were evaluated, and the thermoelectric properties were measured at four different temperatures.

The following are the conclusions obtained from the results analyzed in this thesis:

- The average grain size value of both pristine SnSe and SnSe with Graphene was approximately the same (~ 10 nm) with narrow grain size distribution.
- Both pristine SnSe and SnSe with Graphene show an enhancement in mechanical properties with hardness values of 1.725±0.002 GPa and 1.496±0.051 GPa respectively, compared to 0.27 GPa obtained in previous study.
- It appears from the electrical resistivity data that the addition of Graphene increased the charge density which enhanced the electrical conductivity of SnSe.
- The nanostructuring of SnSe contributed in scattering charge carriers and a high Seebeck coefficient of 723 μV/K at 373 and 1032 μV/K at 873K was achieved. these values are the highest reported so far according to our literature search.
- The addition of Graphene to the pristine SnSe contributed to lowering the thermal conductivity by 21% in average by creating additional phonon scattering centers.
- The nanostructuring in pristine SnSe appeared to enhance the thermoelectric properties that results in a significant improvement of the ZT value to 0.9 at 873 K.

- The addition of 0.5 wt% of Graphene increased the ZT by around 33% to 1.2 at 873 K. The enhanced ZT value could be related to the increase in power factor.
- Graphene is mainly present around the grain boundaries and it is the first ever reported evidence to identify the location of graphene in a nanocrystalline TE material.

These extraordinarily results are obtained without any doping of the base SnSe material and it is expected for the ZT to further improve with doping.

Future Work

The goal is to reach a ZT value more than 2, the following is the future plan for this work.

- Graphene composition optimization
- Elemental doping
- Device fabrication

REFERENCES

[1] "U.S. Energy Information Administration (EIA)." [Online]. Available: https://www.eia.gov/. [Accessed: 14-Apr-2018].

[2] T. M. Tritt, "Thermoelectric Phenomena, Materials, and Applications," *Annu. Rev. Mater. Res.*, vol. 41, no. 1, pp. 433–448, 2011.

[3] M. Martín-González, O. Caballero-Calero, and P. Díaz-Chao, "Nanoengineering thermoelectrics for 21st century: Energy harvesting and other trends in the field," *Renew. Sustain. Energy Rev.*, vol. 24, pp. 288–305, 2013.

[4] M. Hamid Elsheikh *et al.*, "A review on thermoelectric renewable energy: Principle parameters that affect their performance," *Renew. Sustain. Energy Rev.*, vol. 30, pp. 337–355, 2014.

[5] Fitriani *et al.*, "A review on nanostructures of high-temperature thermoelectric materials for waste heat recovery," *Renew. Sustain. Energy Rev.*, vol. 64, pp. 635–659, 2016.

[6] L. Das, A. Guleria, S. Neogy, and S. Adhikari, "Porous nanostructures of SnSe: role of ionic liquid, tuning of nanomorphology and mechanistic studies," *RSC Adv.*, vol. 6, no. 95, pp. 92934–92942, 2016.

[7] H. Ju and J. Kim, "Effect of SiC ceramics on thermoelectric properties of SiC/SnSe composites for solid-state thermoelectric applications," *Ceram. Int.*, vol. 42, no. 8, pp. 9550–9556, 2016.

[8] L.-D. Zhao *et al.*, "Ultralow thermal conductivity and high thermoelectric figure of merit in SnSe crystals," *Nature*, vol. 508, no. 7496, pp. 373–377, 2014.

[9] L.-D. Zhao, V. P. Dravid, and M. G. Kanatzidis, “The panoscopic approach to high performance thermoelectrics,” *Energy Environ. Sci.*, vol. 7, no. 1, pp. 251–268, 2014.

[10] X. Zhang and L.-D. Zhao, “Thermoelectric materials: Energy conversion between heat and electricity,” *J. Mater.*, vol. 1, no. 2, pp. 92–105, 2015.

[11] S. Based, O. N. The, and S. Effect, “Sensors based on the seebeck effect,” vol. 10, pp. 321–346, 1986.

[12] G. S. Nolas, J. Sharp, and H. J. Goldsmid, *Thermoelectrics Basic Principles and New Materials Developments*. 2001.

[13] A. W. Van Herwaarden, “The seebeck effect in silicon ICs,” *Sensors and Actuators*, vol. 6, no. 4, pp. 245–254, 1984.

[14] J. F. Li, W. S. Liu, L. D. Zhao, and M. Zhou, “High-performance nanostructured thermoelectric materials,” *NPG Asia Mater.*, vol. 2, no. 4, pp. 152–158, 2010.

[15] *Thermoelectric refrigaration*. .

[16] H. Alam and S. Ramakrishna, “A review on the enhancement of figure of merit from bulk to nano-thermoelectric materials,” *Nano Energy*, vol. 2, no. 2, pp. 190–212, 2013.

[17] I. Terasaki, *Introduction to thermoelectricity*, *Springer*, vol. 121, 2005.

[18] Y. Wu, S. W. Finefrock, and H. Yang, “Nanostructured thermoelectric: Opportunities and challenges,” *Nano Energy*, vol. 1, no. 5, pp. 651–653, 2012.

[19] W. Liu, X. Yan, G. Chen, and Z. Ren, “Recent advances in thermoelectric nanocomposites,” *Nano Energy*, vol. 1, no. 1, pp. 42–56, 2012.

[20] Z. G. Chen, G. Hana, L. Yanga, L. Cheng, and J. Zou, “Nanostructured

thermoelectric materials: Current research and future challenge," *Prog. Nat. Sci. Mater. Int.*, vol. 22, no. 6, pp. 535–549, 2012.

[21] J. R. Sootsman, D. Y. Chung, and M. G. Kanatzidis, "New and old concepts in thermoelectric materials," *Angew. Chemie - Int. Ed.*, vol. 48, no. 46, pp. 8616–8639, 2009.

[22] N. Oeschler, S. Hartmann, U. Koehler, M. Deppe, P. Sun, and F. Steglich, "Properties and Applications of Thermoelectric Materials," pp. 81–90, 2009.

[23] C. Gayner and K. K. Kar, "Recent advances in thermoelectric materials," *Prog. Mater. Sci.*, vol. 83, pp. 330–382, 2016.

[24] S. K. Bux, J.-P. Fleurial, and R. B. Kaner, "Nanostructured materials for thermoelectric applications," *Chem. Commun.*, vol. 46, no. 44, p. 8311, 2010.

[25] M. Beekman, D. T. Morelli, and G. S. Nolas, "Better thermoelectrics through glass-like crystals," *Nat. Mater.*, vol. 14, no. 12, pp. 1182–1185, 2015.

[26] G. Chen, M. S. Dresselhaus, G. Dresselhaus, J.-P. Fleurial, and T. Caillat, "Recent developments in thermoelectric materials," *Int. Mater. Rev.*, vol. 48, no. 1, pp. 45–66, 2003.

[27] M. G. Kanatzidis, "Nanostructured thermoelectrics: The new paradigm?," *Chem. Mater.*, vol. 22, no. 3, pp. 648–659, 2010.

[28] W. Inst, C. Uk, and W. Inst, "Phonon scattering at grain boundaries in heavily doped fine-grained silicon-germanium alloys," vol. I, p. 16, 1981.

[29] A. S. Henry and G. Chen, "Spectral Phonon Transport Properties of Silicon Based on Molecular Dynamics Simulations and Lattice Dynamics," vol. 5, no. 2, pp. 1–12, 2008.

[30] Y. Li *et al.*, “Enhanced mid-temperature thermoelectric performance of textured SnSe polycrystals made of solvothermally synthesized powders,” *J. Mater. Chem. C*, vol. 4, no. 10, pp. 2047–2055, 2016.

[31] F. K. Butt, B. Ul Haq, S. ur Rehman, R. Ahmed, C. Cao, and S. AlFaifi, “Investigation of thermoelectric properties of novel cubic phase SnSe: A promising material for thermoelectric applications,” *J. Alloys Compd.*, vol. 715, pp. 438–444, 2017.

[32] S. Yang *et al.*, “Highly-anisotropic optical and electrical properties in layered SnSe,” *Nano Res.*, vol. 11, no. 1, pp. 554–564, 2017.

[33] I. U. Atsushi Okazaki, “The crystal structure of Stannous Selenide SnSe,” *J. Phys. Soc. Japan*, vol. 11, no. 4, pp. 470–470, 1956.

[34] H. Wiedemeier and H. G. Von Schnering, “Refinement of the structures of GeS , GeSe , SnS and SnSe,” vol. 303, pp. 295–303, 1978.

[35] F. J. C. HERIBERT WIEDEMEIER, “EQUILIBRIUM SUBLIMATION AND THERMODYNAMIC PROPERTIES OF SnS*,” *Thermochim. Acta*, vol. 34, pp. 257–265, 1979.

[36] B. Zhang *et al.*, “The chemistry and structural thermal stability of hole-doped single crystalline SnSe,” *J. Alloys Compd.*, vol. 688, pp. 1088–1094, 2016.

[37] C. Li *et al.*, “Excellent thermoelectricity performance of p-type SnSe along b axis,” *Phys. B Condens. Matter*, vol. 530, no. November 2017, pp. 264–269, 2018.

[38] K. Tyagi *et al.*, “Electrical transport and mechanical properties of thermoelectric tin selenide,” *RSC Adv.*, vol. 6, no. 14, pp. 11562–11569, 2016.

[39] S. Sassi *et al.*, “Assessment of the thermoelectric performance of polycrystalline p-

type SnSe," *Appl. Phys. Lett.*, vol. 212105, pp. 21–25, 2014.

[40] Y. Li, B. He, J. P. Heremans, and J.-C. Zhao, "High-temperature oxidation behavior of thermoelectric SnSe," *J. Alloys Compd.*, vol. 669, pp. 224–231, 2016.

[41] F. Serrano-Sánchez, N. M. Nemes, O. J. Dura, M. T. Fernandez-Diaz, J. L. Martínez, and J. A. Alonso, "Structural phase transition in polycrystalline SnSe: A neutron diffraction study in correlation with thermoelectric properties," *J. Appl. Crystallogr.*, vol. 49, no. 6, pp. 2138–2144, 2016.

[42] F. Serrano-Sánchez, M. Gharsallah, N. M. Nemes, F. J. Mompean, J. L. Martínez, and J. A. Alonso, "Record Seebeck coefficient and extremely low thermal conductivity in nanostructured SnSe," *Appl. Phys. Lett.*, vol. 106, no. 8, 2015.

[43] W. H. Chen, Z. R. Yang, F. H. Lin, and C. J. Liu, "Nanostructured SnSe: hydrothermal synthesis and disorder-induced enhancement of thermoelectric properties at medium temperatures," *J. Mater. Sci.*, vol. 52, no. 16, pp. 9728–9738, 2017.

[44] Y. Fu, J. Xu, G. Liu, J. Yang, X. Tan, and Z. Liu, "Enhanced thermoelectric performance in p-type polycrystalline SnSe benefiting from," *J. Mater. Chem. C*, vol. 4, pp. 1201–1207, 2016.

[45] D. Feng *et al.*, "Enhanced thermoelectric properties of SnSe polycrystals via texture control," *Phys. Chem. Chem. Phys. Phys. Chem. Chem. Phys*, vol. 18, no. 18, pp. 31821–31827, 2016.

[46] F. Li *et al.*, "Enhanced Thermoelectric Properties of Polycrystalline SnSe via LaCl3 Doping," *Materials (Basel).*, vol. 11, no. 2, p. 203, 2018.

[47] J. Gao and G. Xu, "Intermetallics Thermoelectric performance of polycrystalline Sn

1- x Cu x Se (x = 0 – 0 . 03) prepared by high pressure method," *Intermetallics*, vol. 89, no. March, pp. 40–45, 2017.

[48] D. Li, X. Tan, J. Xu, G. Liu, M. Jin, and H. Shao, "Enhanced thermoelectric performance in n-type polycrystalline SnSe by PbBr 2 doping," *RSC Adv.*, vol. 7, pp. 17906–17912, 2017.

[49] Y. Fu *et al.*, "Study on Thermoelectric Properties of Polycrystalline SnSe by Ge Doping," *J. Electron. Mater.*, vol. 46, no. 5, pp. 3182–3186, 2017.

[50] J. C. Li, D. Li, X. Y. Qin, and J. Zhang, "Enhanced thermoelectric performance of p-type SnSe doped with Zn," *Scr. Mater.*, vol. 126, pp. 6–10, 2017.

[51] J. O. Morales Ferreiro *et al.*, "Effect of the annealing on the power factor of un-doped cold-pressed SnSe," *Appl. Therm. Eng.*, vol. 111, pp. 1426–1432, 2017.

[52] C. Chang *et al.*, "Raising thermoelectric performance of n-type SnSe via Br doping and Pb alloying," *RSC Adv.*, vol. 6, no. 100, pp. 98216–98220, 2016.

[53] G. Tang *et al.*, "Realizing High Figure of Merit in Phase-Separated Polycrystalline Sn 1 −," 2016.

[54] T. Wei, G. Tan, X. Zhang, C. Wu, J. Li, and V. P. Dravid, "Distinct Impact of Alkali-Ion Doping on Electrical Transport Properties of Thermoelectric p - Type Polycrystalline SnSe," 2016.

[55] J. C. Li, D. Li, W. Xu, X. Y. Qin, Y. Y. Li, and J. Zhang, "Enhanced thermoelectric performance of SnSe based composites with carbon black nanoinclusions," *Appl. Phys. Lett.*, vol. 109, no. 17, pp. 1–5, 2016.

[56] H.-Q. Leng, M. Zhou, J. Zhao, Y.-M. Han, and L.-F. Li, "The thermoelectric performance of anisotropic SnSe doped with Na," *RSC Adv.*, vol. 6, no. 11, pp.

9112–9116, 2016.

[57] S. R. Popuri, M. Pollet, R. Decourt, F. D. Morrison, N. S. Bennett, and J. W. G. Bos, "Large thermoelectric power factors and impact of texturing on the thermal conductivity in polycrystalline SnSe," *J. Mater. Chem. C*, vol. 4, no. 8, pp. 1685–1691, 2016.

[58] J. H. Kim *et al.*, "Indium substitution effect on thermoelectric and optical properties of Sn1-xInxSe compounds," *J. Alloys Compd.*, vol. 682, pp. 785–790, 2016.

[59] N. K. Singh, S. Bathula, B. Gahtori, K. Tyagi, D. Haranath, and A. Dhar, "The effect of doping on thermoelectric performance of p-type SnSe: Promising thermoelectric material," *J. Alloys Compd.*, vol. 668, pp. 152–158, 2016.

[60] H. Liu, X. Zhang, S. Li, Z. Zhou, Y. Liu, and J. Zhang, "Synthesis and Thermoelectric Properties of SnSe by Mechanical Alloying and Spark Plasma Sintering Method," *J. Electron. Mater.*, vol. 46, no. 5, pp. 0–4, 2016.

[61] J. Yang, G. Zhang, G. Yang, C. Wang, and Y. X. Wang, "Outstanding thermoelectric performances for both p- and n-type SnSe from first-principles study," *J. Alloys Compd.*, vol. 644, pp. 615–620, 2015.

[62] Z. H. Ge, K. Wei, H. Lewis, J. Martin, and G. S. Nolas, "Bottom-up processing and low temperature transport properties of polycrystalline SnSe," *J. Solid State Chem.*, vol. 225, pp. 354–358, 2015.

[63] Q. Zhang, E. K. Chere, J. Sun, F. Cao, K. Dahal, and S. Chen, "Studies on Thermoelectric Properties of n-type Polycrystalline SnSe 1- x S x by Iodine Doping," *Adv. Energy Mater.*, no. 400, pp. 1–8, 2015.

[64] T.-R. Wei *et al.*, "Thermoelectric transport properties of pristine and Na-doped SnSe

1−x Te x polycrystals," *Phys. Chem. Chem. Phys.*, vol. 17, no. 44, pp. 30102–30109, 2015.

[65] Y. Li, X. Shi, D. Ren, J. Chen, and L. Chen, "Investigation of the anisotropic thermoelectric properties of oriented polycrystalline SnSe," *Energies*, vol. 8, no. 7, pp. 6275–6285, 2015.

[66] C.-L. Chen, H. Wang, Y.-Y. Chen, T. Day, and G. J. Snyder, "Thermoelectric properties of p-type polycrystalline SnSe doped with Ag," *J. Mater. Chem. A*, vol. 2, no. 29, pp. 11171–11176, 2014.

[67] E. K. Chere, Q. Zhang, K. Dahal, F. Cao, J. Mao, and Z. Ren, "Studies on thermoelectric figure of merit of Na-doped p-type polycrystalline SnSe," *J. Mater. Chem. A*, vol. 4, no. 5, pp. 1848–1854, 2016.

[68] M. Gharsallah, F. Serrano-Sánchez, N. M. Nemes, F. J. Mompeán, J. L. Martínez, M. T. Fernández-Díaz, F. Elhalouani, and J. A. Alonso., "Giant Seebeck effect in Ge-doped SnSe," *Sci. Rep.*, vol. 6, no. May, pp. 1–9, 2016.

[69] Y. Gong, C. Chang, W. Wei, J. Liu, W. Xiong, S. Chai, D. Li, J. Zhang, and G. Tang., "Extremely low thermal conductivity and enhanced thermoelectric performance of polycrystalline SnSe by Cu doping," *Scr. Mater.*, vol. 147, pp. 74–78, 2018.

[70] D. Li, J. Li, X. Qin, J. Zhang, H. Xin, C. Song, and L. Wang., "Enhanced thermoelectric performance in SnSe based composites with PbTe nanoinclusions," *Energy*, vol. 116, pp. 861–866, 2016.

[71] J. Gao, H. Zhu, T. Mao, L. Zhang, J. Di, and G. Xu, "The effect of Sm doping on the transport and thermoelectric properties of SnSe," *Mater. Res. Bull.*, vol. 93, pp.

366–372, 2017.

[72] Z.-H. Ge, D. Song, X. Chong, F. Zheng, L. Jin, X. Qian, L. Zheng, R. E. Dunin-Borkowski, P. Qin, J. Feng, and L.-D. Zhao., "Boosting the Thermoelectric Performance of (Na , K) -Codoped Polycrystalline SnSe by Synergistic Tailoring of the Band Structure and Atomic-Scale Defect Phonon Scattering," pp. 6–12, 2017.

[73] F. Li, W. Wang, X. Qiu, Z. Zheng, P. Fan, J. Luo, and B. Li., "Optimization of thermoelectric properties of n-type Ti, Pb co-doped SnSe," *Inorg. Chem. Front.*, vol. 4, no. 10, pp. 1721–1729, 2017.

[74] H. Guo, H. Xin, X. Qin, J. Zhang, D. Li, Y. Li, C. Song, and C. Li., "Enhanced thermoelectric performance of highly oriented polycrystalline SnSe based composites incorporated with SnTe nanoinclusions," *J. Alloys Compd.*, vol. 689, pp. 87–93, 2016.

[75] T. A. Wubieneh, C.-L. Chen, P. C. Wei, S.-Y. Chen, "The effects of Ge doping on the thermoelectric performance of p-type polycrystalline SnSe," *RSC Adv.*, vol. 6, no. 115, pp. 114825–114829, 2016.

[76] Y.-M. Han, J. Zhao, M. Zhou, X.-X. Jiang, H.-Q. Leng, and L.-F. Li, "Thermoelectric performance of SnS and SnS–SnSe solid solution," *J. Mater. Chem. A*, vol. 3, no. 8, pp. 4555–4559, 2015.

[77] A. Banik and K. Biswas, "Lead-free thermoelectrics: promising thermoelectric performance in p-type SnTe1−xSex system," *J. Mater. Chem. A*, vol. 2, no. JUNE, p. 9620, 2014.

[78] T. A. Amollo, G. T. Mola, M. S. K. Kirui, and V. O. Nyamori, "Graphene for Thermoelectric Applications: Prospects and Challenges," *Crit. Rev. Solid State*

Mater. Sci., pp. 1–25, 2017.

[79] Ponnamma, D. and Kumar Sadasivuni, K. "Graphene/Polymer Nanocomposites: Role in Electronics," *Graphene-Based Polymer Nanocomposites in Electronics*. Springer, pp.1-24, 2015.

[80] P. Dollfus, V. H. Nguyen, and J. Saint-Martin, "Thermoelectric effects in graphene nanostructures," *J. Phys. Condens. Matter*, vol. 27, no. 13, 2015.

[81] Z. Y. U. Juang, C. C. Tseng, C. H. Chen, L. J. Li, and M. Sciences, "Graphene-Based Thermoelectric Materials," *AAPPS Bull.*, vol. 23, no. 4, pp. 14–18, 2013.

[82] D. Dragoman and M. Dragoman, "Giant thermoelectric effect in graphene," *Appl. Phys. Lett.*, vol. 91, no. 20, pp. 1–4, 2007.

[83] Y. M. Zuev, W. Chang, and P. Kim, "Thermoelectric and magnetothermoelectric transport measurements of graphene," *Phys. Rev. Lett.*, vol. 102, no. 9, pp. 1–4, 2009.

[84] Y. Ouyang and J. Guo, "A theoretical study on thermoelectric properties of graphene nanoribbons," *Appl. Phys. Lett.*, vol. 94, no. 26, 2009.

[85] H. Sevinçli and G. Cuniberti, "Enhanced thermoelectric figure of merit in edge-disordered zigzag graphene nanoribbons," *Phys. Rev. B*, vol. 81, no. 11, p. 113401, 2010.

[86] Y. Du, S. Z. Shen, W. Yang, R. Donelson, K. Cai, and P. S. Casey, "Simultaneous increase in conductivity and Seebeck coefficient in a polyaniline/graphene nanosheets thermoelectric nanocomposite," *Synth. Met.*, vol. 161, no. 23–24, pp. 2688–2692, 2012.

[87] B. Liang, Z. Song, M. Wang, L. Wang, and W. Jiang, "Fabrication and

Thermoelectric Properties of Graphene/ Composite Materials," *J. Nanomater.*, vol. 2013, pp. 1–5, 2013.

[88] A. Rahman, A. Umar, X. Chen, M. Salleh, and M. Oyama, "Enhanced thermoelectric properties of bismuth telluride organic hybrid films via graphene doping," *Appl. Phys. A Mater. Sci. Process.*, vol. 122, no. 2, pp. 1–8, 2016.

[89] H. Ju and J. Kim, "Preparation and structure dependent thermoelectric properties of nanostructured bulk bismuth telluride with graphene," *J. Alloys Compd.*, vol. 664, pp. 639–647, 2016.

[90] D. Suh, S. Lee, H. Mun, S.H. Park., "Enhanced thermoelectric performance of Bi0.5Sb1.5Te3-expanded graphene composites by simultaneous modulation of electronic and thermal carrier transport," *Nano Energy*, vol. 13, pp. 67–76, 2015.

[91] D. Zhao, X. Wang, and D. Wu, "Enhanced Thermoelectric Properties of Graphene/Cu2SnSe3 Composites," *Crystals*, vol. 7, no. 3, p. 71, 2017.

[92] H. Ju and J. Kim, "Preparation and structure dependent thermoelectric properties of nanostructured bulk bismuth telluride with graphene," *J. Alloys Compd.*, vol. 664, pp. 639–647, 2016.

[93] C. Suryanarayana, "Synthesis of nanocomposites by mechanical alloying," *J. Alloys Compd.*, vol. 509, no. SUPPL. 1, pp. S229–S234, 2011.

[94] C. Suryanarayana, "Mechanical alloying and milling," *Prog. Mater. Sci.*, vol. 46, no. 1–2, pp. 1–184, 2001.

[95] U. Anselmi-Tamburini, J. E. Garay, and Z. A. Munir, "Fundamental investigations on the spark plasma sintering/synthesis process," *Mater. Sci. Eng. A*, vol. 407, no. 1–2, pp. 24–30, 2005.

[96] V. Accordingly and I. Boxes, “Principles of X-ray Diffraction,” *Willey*, pp. 1-41, 2006.

[97] Callister, W. D., & Rethwisch, D. G. “Fundamentals of materials science and engineering: An integrated approach,” *Hoboken, NJ: Wiley. 2012.*

[98] L. E. KLUNG, H. P.; ALEXANDER, “X-ray diffraction procedures,” *Willey, New York, EUA*, p. 491, 1962.

[99] D. B. Williams and C. B. Carter, *Transmission Electron Microscopy: A Textbook for Materials Science*, vol. 1–4. 2009.

[100] L. A. Giannuzzi and F. A. Stevie, “A review of focused ion beam milling techniques for TEM specimen preparation,” *Micron*, vol. 30, no. 3, pp. 197–204, 1999.

[101] P. D. Nellist, “The Principles of STEM Imaging,” in *Scanning Transmission Electron Microscopy*, 2011, pp. 91–115.

[102] Y. Kong and J. N. Hay, “The measurement of the crystallinity of polymers by DSC,” *Polymer (Guildf).*, vol. 43, no. 14, pp. 3873–3878, 2002.

[103] S. A. Shahdad, J. F. McCabe, S. Bull, S. Rusby, and R. W. Wassell, “Hardness measured with traditional Vickers and Martens hardness methods,” *Dent. Mater.*, vol. 23, no. 9, pp. 1079–1085, 2007.

[104] W. Qin and J. A. Szpunar, “Origin of lattice strain in nanocrystalline materials,” *Philos. Mag. Lett.*, vol. 85, no. 12, pp. 649–656, 2005.

[105] S. Lv, Z. Ge, Y. Chen, K.Zhao, J. Feng, J. He., “Thermoelectric properties of polycrystalline $SnSe_{1\pm x}$ prepared by mechanical alloying and spark plasma sintering,” *RSC Adv.*, vol. 6, no. 95, pp. 92335–92340, 2016.

[106] R. He, S. Gahlawat, C. Guo, S. Chen., “Studies on mechanical properties of

thermoelectric materials by nanoindentation," *Phys. Status Solidi*, vol. 212, no. 10, pp. 2191–2195, 2015.

[107] J. Schiotz, F. D. Di Tolla, and K. W. Jacobsen, "Softening of nanocrystalline metals at very small grain sizes," *Nature*, vol. 391, no. February, pp. 561–563, 1998.

[108] J. Schioøtz and K. W. Jacobsen, "A maximum in the strength of nanocrystalline copper," *Science.*, vol. 301, no. 5638, pp. 1357–1359, 2003.